A Capacitor Coupled On-board Bi-directional Vehicle-to-Vehicle Charging System

Mounika Reddimalla, and Srinivasan Pradabane, *Member, IEEE*

***Abstract*—In recent times, Vehicle-to-Vehicle (V2V) chargers have gained popularity to transfer the energy between two Electric Vehicles (EVs). In this paper, a new direct V2V charger is proposed that uses a capacitor coupling and an on-board DC-DC converter in each EV to enable the energy transfer between them. Importantly, this charger differentiates itself from other V2V chargers by eliminating the requirement for motor winding and inverter circuit from an EV. The charger operation is verified through simulation studies (via MATLAB/Simulink®) in three operating modes: Forward Boost, Reverse Buck and Forward Buck-Boost mode for EV's with battery voltage of 350 V and 450 V. The simulation studies are validated through the OPAL-RT® Real-Time simulator. The proposed charger achieves an efficiency of 96.57 % in the forward boost mode, 96.56 % in the reverse buck mode, and 96.26 % in the forward buck–boost mode of operation at a rated power level of 20 kW, while demonstrating a 25 % to 76 % reduction in component count compared to existing topologies. Further, a laboratory proof of concept is developed and tested with battery voltages of 12 V and 25.6 V in all modes of operation. Experimental results under static and dynamic discharge currents are presented.**

Link to graphical and video abstracts, and to code:
https://latamt.ieeer9.org/index.php/transactions/article/view/10076

***Index Terms*—Battery charging, Bi-directional power transfer, Conductive charging, Electric Vehicle, Vehicle-to-Vehicle (V2V)**

I. Introduction

ELECTRIC Vehicles (EVs) are being recognized as a potential substitute for fuel-based automobiles to reduce emissions of greenhouse gases in urban areas [1]–[5]. The only energy source available to run the EV's motors is the battery bank. Conventionally, the battery in an EV is charged from an AC/DC grid by using an off-board Grid-to-Vehicle (G2V) charger [3]–[5]. Various G2V arrangements used in the charging stations along with different levels of charging rates are discussed in the literature [4]–[10]. Partial Power Processing (PPP) based G2V topologies [11]–[14] are presented for fast charging applications with enhanced conversion efficiency. Off-board PPP based G2V chargers [11], [12] are designed for DC micro grid to EV charging stations, whereas the G2V chargers [13], [14] presented the on-board AC Grid to EV chargers. Integrated on-board G2V charger is presented [6] by utilizing on-board inverter and motor windings. In G2V mode, charging a high concentration of EVs simultaneously can strain the grid, hence leading to grid stability issues [5]. In-order to address this issue, a bi-directional charger [8], [21] is presented, which can also transfer the energy from Vehicle-to-Grid (V2G) along with G2V operation. A V2G/G2V algorithm [7] is proposed to co-ordinate and schedule charging and discharging time among the connected EVs. Hence, it reduces the overload on grid and optimize the total charging energy and cost of an EV. Military-based EVs form a micro-grid by V2G operation is presented in [17], which helps to power up the military base and other ancillary activities. It also emphasizes the Vehicle-to-Vehicle (V2V) power transfer in combat and emergency situations. Recent times, many commercial EVs are providing the V2V and Vehicle-to-Load (V2L) power transfer features. For example, due to low battery a stranded Hyundai Kona EV was supported by another EV through V2V operation, which reduce the range anxiety of EV owners. A review of commercial EVs with V2V features and a communication framework required for their co-ordination is extensively explained in [18].

The V2V chargers are broadly classified as: 1) In-direct charging [15], [16], [19] and 2) Direct charging [16], [20]–[29]. Indirect mode of charging involves interconnection of two EVs via the utility grid and perform the V2G and G2V operations using an in-built on-board charger. The architecture typically involves a back-end DC-DC converter for the battery interface and a front-end AC-DC converter for the power grid interface. These multiple power conversion stages significantly reduces the V2V power transfer efficiency [16], [19].

The direct power transfer method overcomes this limitation by providing an architecture that facilitates direct V2V power exchange, thereby eliminating the need for an intermediate grid connection [16], [20]. The direct mode of charging encompasses the connection of two EVs via the AC side of each on-board battery charger and the DC side of each on-board charger as presented in literature [16]. In this case, EVs connected through the AC-link of the on-board charger involve four conversion stages, resulting in a reduction in efficiency compared to the DC side. Therefore, connecting the EVs to the DC terminals is advantageous because the batteries require DC power; eliminating the need for DC-AC and AC-DC power conversion. This can be accomplished by either by utilizing the on-board DC-DC converters of the two EVs and connecting them back-to-back, or connecting the battery ports of the two EVs using a separate DC-DC converter.

A concept of Plug-in Electric Vehicle Battery Charging System (PEVBCS) utilizing a bipolar DC power grid is discussed in [19]. This method explains the V2V charging mode along with the facility to charge the vehicle from the grid (G2V) and deliver the power to the grid (V2G). For applications like

The associate editor coordinating the review of this manuscript and approving it for publication was Gabriel Pinto (*Corresponding author: Mounika Reddimalla*).

Mounika Reddimalla, and S. Pradabane are with the National Institute of Technology Warangal, Hanamkonda, Telangana, India (e-mails: rm21eerer03@student.nitw.ac.in, and spradabane@nitw.ac.in).

fast and slow charging stations for EVs, an isolated three-port DC-DC converter based Dual Active Bridge (DAB) converter and a series resonant converter is discussed in literature [20]. This charging provides an isolation and reduction in switching losses by using a resonant circuit. However, it requires an external off-board circuit. Therefore, an increase in the number of components results in a bulky structure, control complexity and a significant reduction in efficiency.

A novel three-port Dual Active Bridge Series Resonant (DABSR) converters are discussed in [21]–[23]. These three ports facilitate the power flow between EVs, PVs, and the grid, but it requires the effective control algorithms to transfer power between EVs, grid and PVs based on the conditions.

A 75-kW direct V2V mobile charging system is discussed in literature [25]. In this charger, the voltage and current stress on the active and passive components and ripples in the output current are lowered by utilizing the interleaved inductors, but the size of the charger increases as the power rating increases to meet the capacity requirement. The size of the charger plays crucial role in automobiles as space is main concern.

Novel EV drive train and motor-integrated charging methods for V2V power transfer are discussed in literature [26], [27]. Bi-directional capabilities of the charger [26] for forward buck and reverse boost modes of operation are demonstrated. The V2V charger [27] is tested only for the buck operation and bypassed the on-board bi-directional buck-boost DC-DC converter. Additionally, switching frequency is varied with respect to the output power to achieve soft switching operation. The neutral points of the three phase traction motor windings of two EVs are connected to establish the interface and the negative rails of drive train of the EV battery are directly connected to one another to create a closed circuit. The high frequency currents in the motor windings leads to the core losses and thereby increases the temperature of the motor windings. Additionally, the large inrush currents in the motor windings will gradually degrades the insulation and thereby reduces the lifespan of EV motor.

In [30], a direct V2V charger bypassing the EV motor is presented. However, it requires a bi-directional converter and inverter for its operation. This direct charging eliminates the burden on the motor and the control of charging is relatively simple. All of the stated above chargers have large components count, control complexity and grid dependency. A direct V2V energy-exchange framework is proposed [33] to reduce the size, control complexity, power overloads in electric grid systems and its associated infrastructure setting up costs.

The following are the distinctive features of the proposed work

- Simple architecture.
- Utilization of fewer number of components in on-board converter.
- Forward and reverse modes of buck, boost, buck-boost operation.
- Coherent Control.

II. Operating Modes Of A V2V Approach and Analysis

The proposed direct V2V charging configuration is depicted in Fig. 1, which uses on-board equipment and an external capacitor C_k for the power transfer between the two EVs. It uses only the on-board battery of voltage V_{b1}, inductor L_1 and switch S_{b1} from EV-1. Similarly, on-board battery of voltage V_{b2}, inductor L_2 and switch S_{b2} from EV-2. The battery currents are denoted by I_{b1} and I_{b2}. The inductor currents of L_1 and L_2 are denoted by I_{L1} and I_{L2}. Capacitor C_k voltage is represented by the V_{ck}. The function of the switches S_{b1} and S_{b2} complement one another.

Assume the power flow direction as "forward" if it flows from EV-1 to EV-2, and as "reverse" if it flows from EV-2 to EV-1. Depending on the voltage levels of two EV batteries, the proposed V2V charger mode of operation is classified as follows:

- *Case A:* EV-1 acting as a sender and EV-2 acting as a receiver and EV-1 voltage is lesser than EV-2 ($V_{b1} < V_{b2}$), then it is referred as "Forward Boost operating mode".
- *Case B:* EV-1 acting as a receiver and EV-2 acting as a sender and EV-1 voltage is lesser than EV-2 ($V_{b1} < V_{b2}$), then it is referred as "Reverse Buck operating mode".
- *Case C:* EV-1 acting as a sender and EV-2 acting as a receiver and EV-1 voltage is equal to EV-2 ($V_{b1} = V_{b2}$), then it is referred as "Forward Buck-Boost operating mode".

A. Forward Boost Mode of Operation:

In this mode, EV-1 functions as a sender and EV-2 functions as a receiver and sender voltage is lesser than receiver ($V_{b1} < V_{b2}$). During the dT_s period, switch S_{b1} turns ON and the switch S_{b2} turns OFF as depicted in Fig. 2(a). Where d is the duty cycle and T_s is the switching time period. In this period, the inductor L_1 gets charged from EV-1 battery and capacitor C_k discharges to transfer energy to EV-2 battery. In $(1-d)T_s$ period, switch S_{b1} turns OFF and S_{b2} turns ON. During this period inductor L_1 gets discharged and the C_k gets charged, as depicted in Fig. 2(b). The analytical waveforms for the proposed charger during forward boost mode of operation are shown in Fig. 3.

The following set of equations during the dT_s period is obtained by applying Kirchhoff's voltage and current rules.

$$\left.\begin{aligned} V_{L1} &= V_{b1} \\ V_{L2} &= V_{b2} - V_{CK} \\ I_{CK} &= I_{L2} \end{aligned}\right\} \rightarrow dT_s \tag{1}$$

$$\left.\begin{aligned} V_{L1} &= V_{b1} - V_{CK} \\ V_{L2} &= V_{b2} \\ I_{CK} &= I_{L1} \end{aligned}\right\} \rightarrow (1-d)T_s \tag{2}$$

The following equations are obtained using the volt-second balance principle for inductors L_1 and L_2.

$$\left.\begin{aligned} V_{b1}dT_s + (V_{b1} - V_{CK})(1-d)T_s &= 0 \\ (V_{b2} - V_{CK})dT_s + (V_{b2})(1-d)T_s &= 0 \end{aligned}\right\} \tag{3}$$

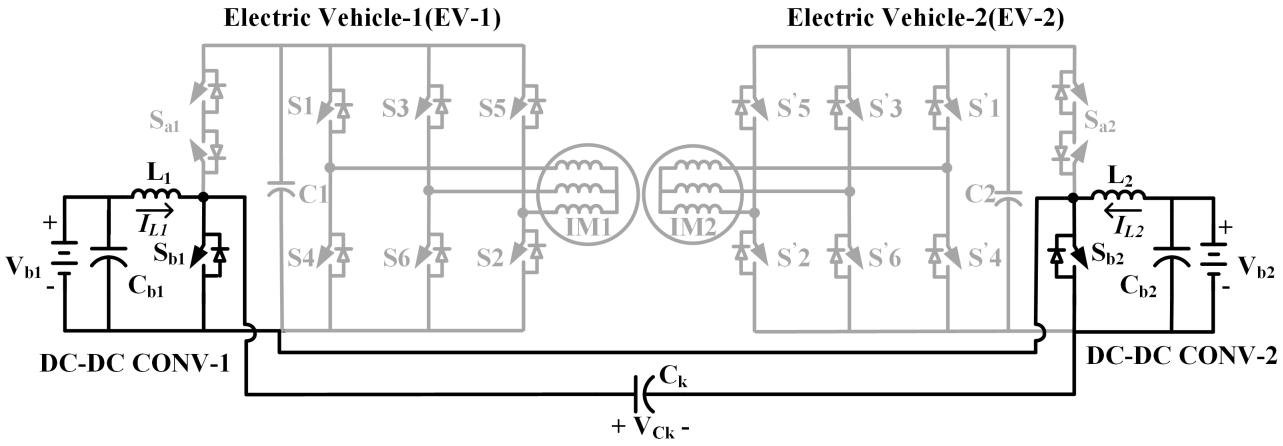

Fig. 1. Proposed V2V charger [33].

solving above equations (3) these equations are obtained.

$$\left.\begin{aligned} V_{CK} &= \frac{V_{b1}}{1-d} \quad = \frac{V_{b2}}{d} \\ \frac{V_{b2}}{V_{b1}} &= \frac{d}{1-d} \end{aligned}\right\} \tag{4}$$

Based on the inductor slope relations, the current ripples of L_1 and L_2 are evaluated. In each switching interval, the inductor current changes as a function of the voltage applied across the inductor and its inductance. Accordingly, the rising and falling current slopes during the ON and OFF intervals are used to derive the inductor current ripple expressions ΔI_{L1}, ΔI_{L2} as presented in equations (5), (6). similarly, the capacitor voltage ripple ΔV_{CK} equation (7) derived.

$$\left.\begin{aligned} V_{L1} &= V_{b1} \\ \Delta I_{L1} &= \frac{V_{b1}}{L_1} \cdot \frac{d}{f_s} \\ V_{L2} &= V_{b2} - V_{CK} \\ \Delta I_{L2} &= \frac{V_{b2} - V_{CK}}{L_2} \cdot \frac{d}{f_s} \end{aligned}\right\} \rightarrow dT_s \tag{5}$$

$$\left.\begin{aligned} V_{L1} &= V_{b1} - V_{CK} \\ \Delta I_{L1} &= \frac{V_{b1} - V_{CK}}{L_1} \cdot \frac{1-d}{f_s} \\ V_{L2} &= V_{b2} \\ \Delta I_{L2} &= \frac{V_{b2}}{L_2} \cdot \frac{1-d}{f_s} \end{aligned}\right\} \rightarrow (1-d)T_s \tag{6}$$

$$\left.\begin{aligned} \Delta V_{CK} &= \frac{1}{C_K}\int_0^{DT_s} I_{CK}(t)\,dt \\ I_{CK} &= I_{L2} \\ \Delta V_{CK} &= \frac{1}{C_K}\int_0^{DT_s} I_{L2}(t)\,dt \quad = I_{L2}\,dT \\ \Delta V_{CK} &= \frac{I_{L2}.d}{C_K f_s} \end{aligned}\right\} \rightarrow dT_s \tag{7}$$

Assume the charger operates in steady-state continuous conduction mode (CCM), the total rising current change over the ON interval equals the total falling current change over the OFF interval. Therefore, the peak–to–peak inductor current ripples ΔI_{L1} and ΔI_{L2} can be computed using either the ON–interval or the OFF–interval expressions. Therefore, the ripple currents of I_{L1} and I_{L2} are ΔI_{L1} and ΔI_{L2} and capacitor voltage V_{CK} ripple ΔV_{CK} is expressed as follows.

$$\left.\begin{aligned} \Delta I_{L1} &= \frac{V_{b1} d}{L_1 f_s} \\ \Delta I_{L2} &= \frac{V_{b2}(1-d)}{L_2 f_s} \\ \Delta V_{CK} &= \frac{I_{L2} d}{C_K f_s} \end{aligned}\right\} \tag{8}$$

B. Reverse Buck Mode of Operation:

In this mode, EV-2 functions as a sender and EV-1 as a receiver and sender voltage is lesser than receiver ($V_{b1} < V_{b2}$). The switch S_{b2} turns ON and the switch S_{b1} turns OFF during the dT_s period as depicted in Fig. 4(a). During this period, the inductor L_2 gets charged from EV-2 battery and capacitor C_k discharges to transfer energy to EV-1 battery. In $(1-d)T_s$ period, switch S_{b1} turns ON and S_{b2} turns OFF. During this period inductor, L_2 gets discharged and the C_k gets charged, as depicted in Fig. 4(b). The analytical waveforms for the proposed charger are shown in Fig. 5.

C. Forward Buck-Boost Mode of Operation:

In this mode, EV-1 functions as a sender and EV-2 functions as a receiver and sender voltage is equal to the receiver (V_{b1} = V_{b2}). The mode of operation is similar to forward boost operation. When the switch S_{b1} turns ON and the switch S_{b2} turns OFF, inductor L_1 gets charged from EV-1 battery and capacitor C_k discharges to transfer energy to EV-2 battery. When the switch S_{b2} turns ON and switch S_{b1} turns OFF, inductor L_1 gets discharged and the C_k gets charged.

D. Battery Modeling:

The structure of the battery equivalent model is illustrated in Fig. 6. In this model, V_b represents the battery terminal voltage, V_{OC} denotes the open-circuit voltage, and V_p correspond to the voltage associated with polarization effect.

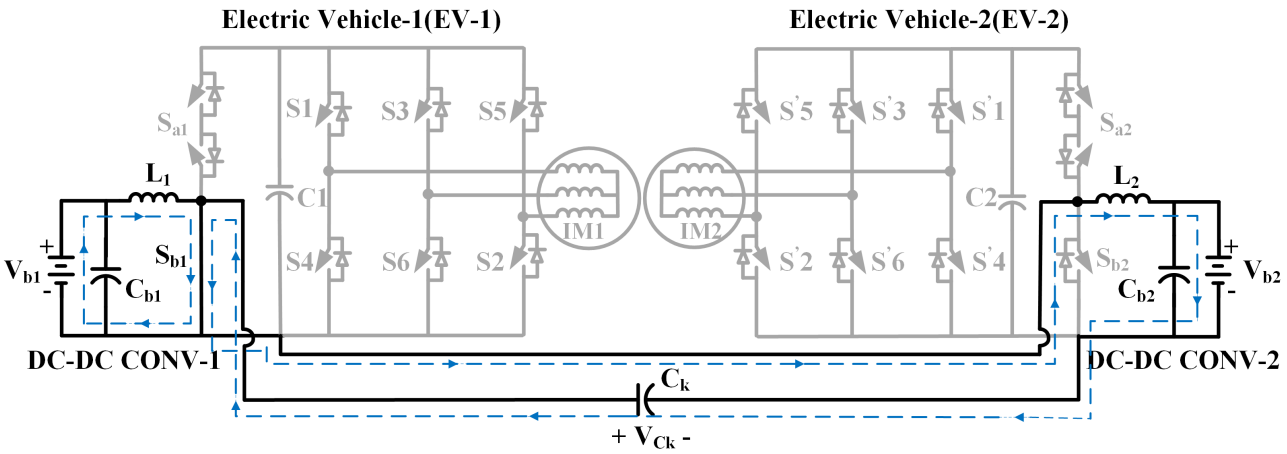

(a)

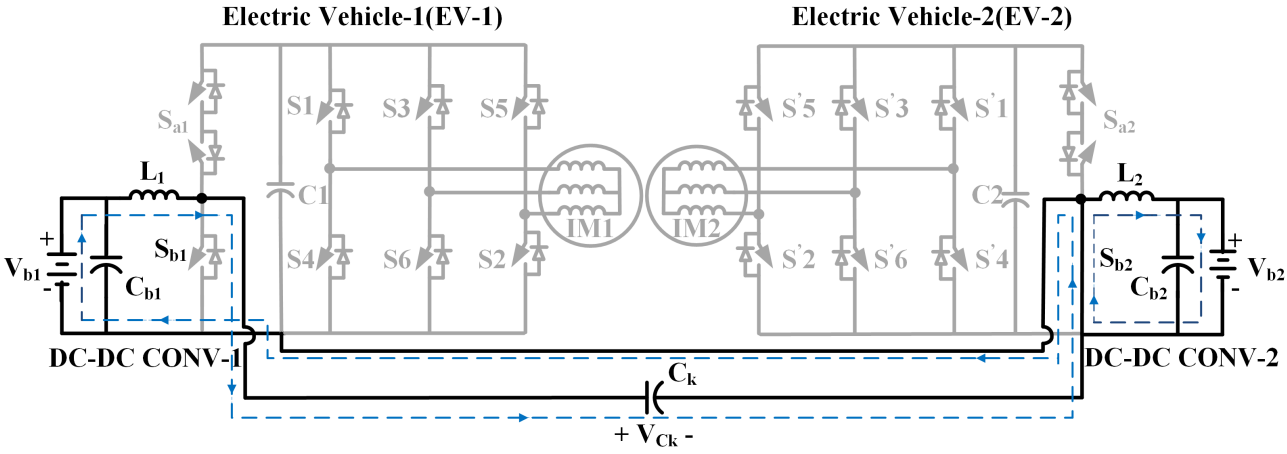

(b)

Fig. 2. Forward boost operation (a) when S_{b1} is ON, (b) when S_{b2} is ON.

The variable I_b indicates the battery current (positive during discharging and negative during charging). The parameters R_0 and R_p represent the internal ohmic and polarization resistances, whereas C_p denote the polarization capacitance. The mathematical representation of battery terminal voltage V_b and SOC equations (9) are given [31] as follows:

$$\left.\begin{aligned} V_{\text{OC}} &= V_b + R_0 I_b + V_p \\ SOC(t) &= SOC(t_0) - \int_{t_0}^{t} \frac{\eta I_b(t)}{Q}\, dt \end{aligned}\right\} \tag{9}$$

The battery state of charge (SOC) depends on the available capacity and the direction of current flow. Here, $SOC(t)$ and $SOC(t_0)$ denote the SOC at times t and t_0, respectively. The parameter η represents the charging/discharging efficiency, and Q is the maximum available capacity of the battery.

E. Stress Analysis on Switches:

The peak voltage across semiconductor devices during their non-conduction mode of operation is known as the voltage stress. In the proposed charger, the voltage stress on each switch S_{b1}, S_{b2} for all operating modes is expressed as follows:

$$V_{Sb1,\max} = V_{Sb2,\max} = V_{CK} = \frac{V_{b1}}{1-d} = \frac{V_{b2}}{d} \Bigg\} \tag{10}$$

The peak current that passes through semiconductor devices during various conduction modes is known as the current stress. In the proposed charger, the current stress on each switch S_{b1}, S_{b2} for all operating modes is expressed as follows:

$$I_{S,\max} = \left(I_{L1} + \frac{\Delta I_{L1}}{2}\right) + \left(I_{L2} + \frac{\Delta I_{L2}}{2}\right) \Bigg\} \tag{11}$$

F. Design of Parameters:

In Forward boost mode of operation, the inductor's value is determined by the switching frequency (f_s), allowable peak-to-peak inductor current ripple, duty cycle, and input supply voltage. Similarly, the capacitor selection is dependent on the maximum permissible voltage ripple (ΔV_{CK}) of the capacitor's operating voltage. To ensure proper design, the inductor's ripple current should be within 5 % to 10 % and capacitor's voltage ripple within 1 % to 5 % is taken into

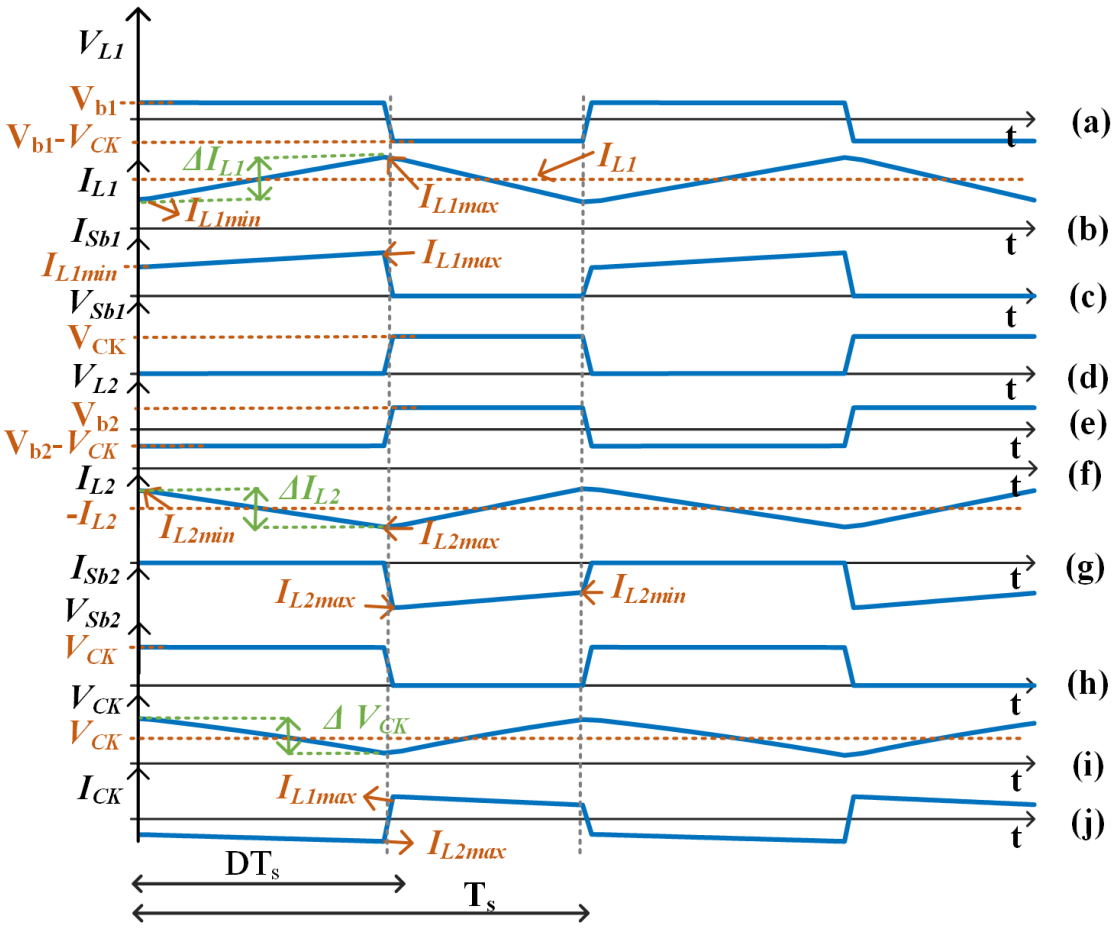

Fig. 3. Analytical waveforms of the proposed charger operating in forward boost mode (a)-(b) Inductor L_1 voltage and current, (c)-(d) Switch S_{b1} current and voltage, (e)-(f) Inductor L_2 voltage and current, (g)-(h) Switch S_{b2} current and voltage, (i)-(j) Capacitor C_k voltage and current.

consideration. From equation (8), the following equation (12) derived for forward boost mode of operation to calculate the L_1, L_2, C_K parameters.

$$\left.\begin{aligned} L_1 &= \frac{V_{b1}d}{\Delta I_{L1} f_s} \\ L_2 &= \frac{V_{b2}(1-d)}{\Delta I_{L2} f_s} \\ C_K &= \frac{I_{L2}d}{\Delta V_{CK} f_s} \end{aligned}\right\} \tag{12}$$

Similar equations are obtained for reverse buck and forward buck-boost mode operation based on sender and receiver parameters.

III. V2V Interface Control Mechanism

A. Control and Communication Workflow:

The Fig. 7 represents the proposed vehicle-to-vehicle (V2V) power sharing algorithm. When two electric vehicles are interconnected through a dedicated V2V cable (CHAdeMO or CCS2), a secure communication handshake is first established via the CAN bus interface. During this handshake, the vehicles exchange essential battery parameters, including state of charge (SOC), nominal voltage, rated capacity, C-rate limits, and the required charging energy for the receiver vehicle. Both vehicles also communicate their instantaneous SOC values and predefined minimum SOC thresholds to ensure that the donor vehicle never discharges below its safe operational limit. Once these parameters are validated, the system commands the closure of the power contactors, enabling controlled energy sharing. The power transfer is maintained under continuous monitoring of current, SOC, voltage deviations, and C-rate constraints. The sharing process automatically terminates once the receiver battery attains the requested charge level, or if any safety-related maximum or minimum threshold is reached, thereby ensuring reliable, safe, and intelligent V2V power exchange.

B. Block Diagram of Control Scheme:

In the proposed charger, to transfer the power between the vehicles, the inductor current of the sender vehicle is taken as a reference. To obtain the required response from the proposed charger, a control scheme is presented in Fig. 8. Here, the inductor current measured at the sending vehicle on-board charger is subtracted from the reference inductor current. The error output from the differentiator is supplied to the controller in order to get the controlled duty ratio. The

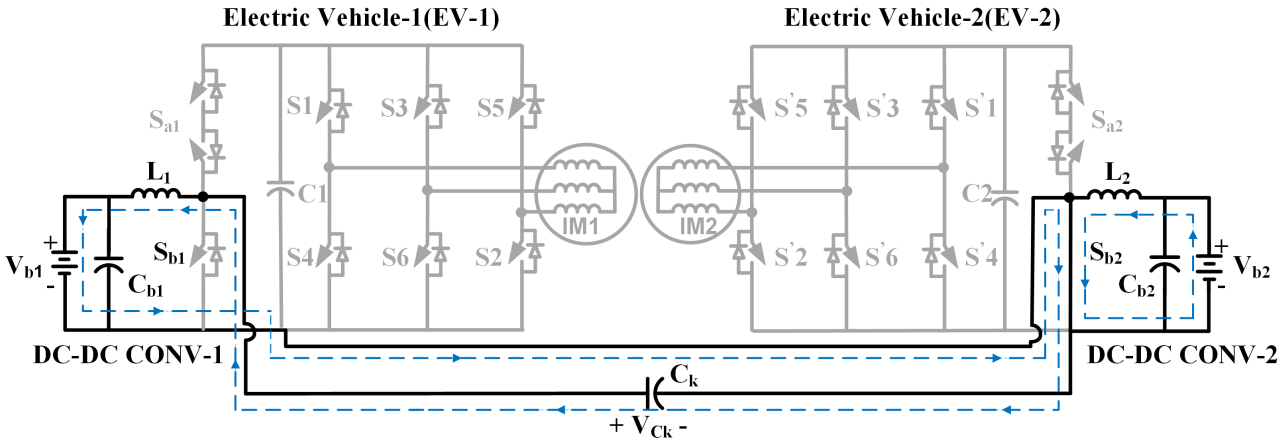

(a)

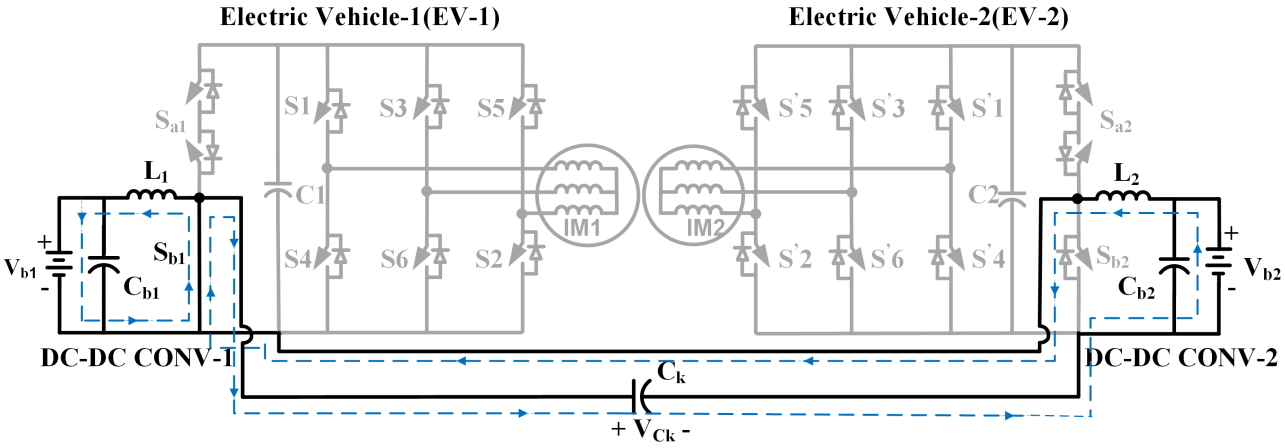

(b)

Fig. 4. Reverse buck operation (a) when S_{b2} is ON, (b) when S_{b1} is ON.

comparator compares the duty ratio with the triangular signal and generates the PWM pulses to switches S_{b1}, and S_{b2}.

C. State Space Analysis:

The controller design and operation play a crucial role in operating the charger effectively as per the requirements. The state space averaging approach (SSA) is used to analyze the stability and control viability of the proposed charger. In accordance with requirements, the suggested direct V2V charger functions in three modes. The inductors L_1, and L_2, and coupled capacitor C_k have internal resistances are R_{L1}, R_{L2} and R_{ck}. The battery-1 open circuit voltage, internal resistance, polarization resistance and capacitance are V_{oc1}, R_{01}, R_{p1}, and C_{p1}. Similarly, battery-2 parameters are V_{oc2}, R_{02}, R_{p2}, and C_{p2} are involved in all three modes of operation. The battery parameters vary with the state of charge (SOC). Therefore, the parameter values at different SOC levels are obtained through the Hybrid Pulse Power Characterization (HPPC) test [31], [32]. The state variables are five based on the inductor current and capacitor voltage in each mode of operation. The following equations are extracted during the forward boost mode of operation.

The average rate of variation of the inductor currents i_{L1}, and i_{L2}, and the capacitor voltages v_{ck}, v_{p1}, and v_{p2} during dT_s and $(1-d)T_s$ is represented in equations (13) and (14). The equations are rearranged in terms of matrix as equations (15) and (16).

The average rate of variation of state and output variables over a cycle is expressed in the equation as (17). The equations are perturbed around the operating point ($x = X + \hat{x}, d = D + \hat{d}, u = U + \hat{u}$). Substituting the perturbations in the state equations and neglecting the non-linear terms and equating steady state and linear terms, the following equation (18) is derived .

$$\left.\begin{aligned} \dot{x} &= Ax + Bu \\ \dot{y} &= Cx + Bu \end{aligned}\right\} \tag{17}$$

Here
x = State variable matrix,
y = Output matrix,
u = Input matrix,
$\wedge$ represents perturbations,
Upper case letter represents DC average value

Applying Laplace transformation to equation (17) and con-

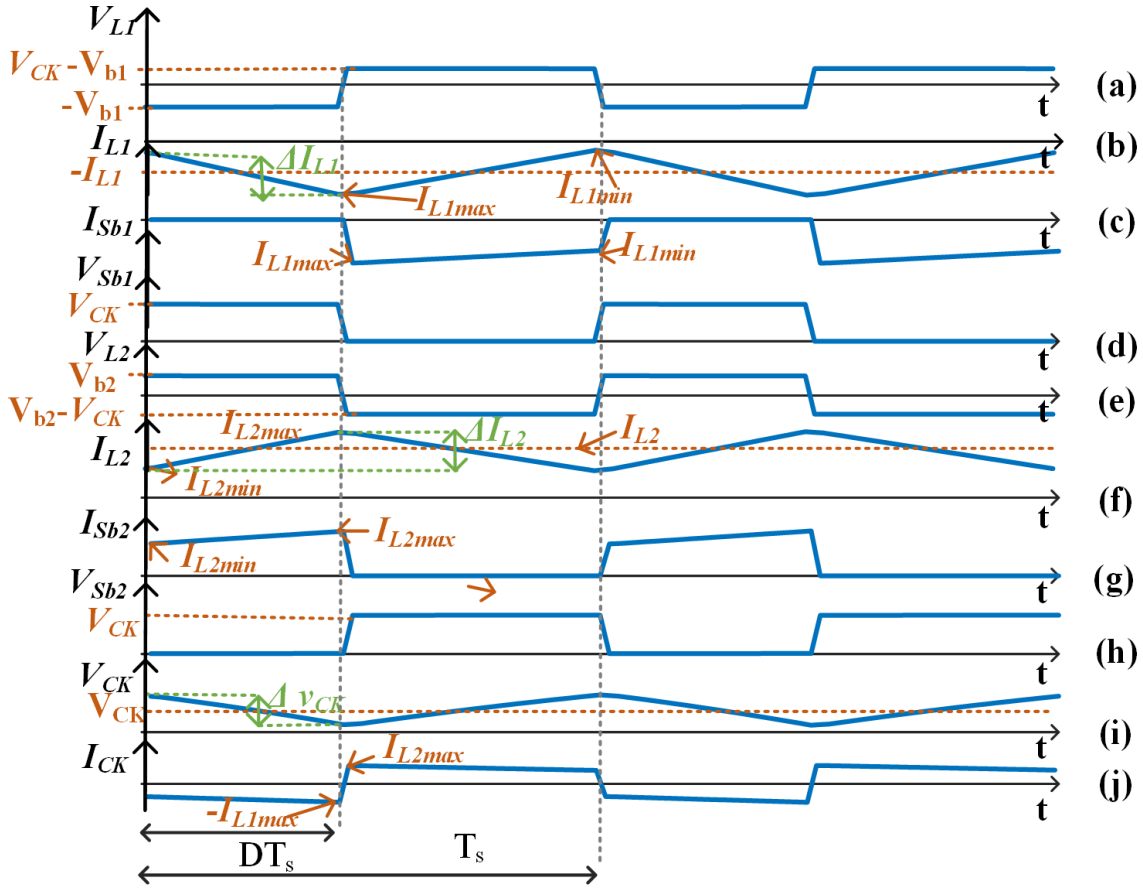

Fig. 5. Analytical waveforms of the proposed charger operating in reverse buck mode (a)-(b) Inductor L_1 voltage and current, (c)-(d) Switch S_{b1} current and voltage, (e)-(f) Inductor L_2 voltage and current, (g)-(h) Switch S_{b2} current and voltage, (i)-(j) Capacitor C_k voltage and current.

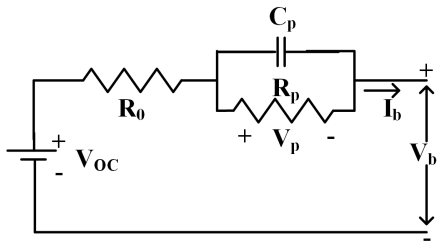

Fig. 6. Battery equivalent circuit model [31].

sidering duty as controlled input $\hat{d}(t)$ in order to obtain the control to output transfer function, is expressed as equation (19).

$$\frac{\hat{y}(s)}{\hat{u}(s)} = C(sI - A)^{-1}B \tag{19}$$

Here, substitute the state matrices and parameters listed in Table I, along with the duty ratio D as 0.617 at 3C rate condition in equation (19). The control to inductor current (i_{L1}) transfer function is derived considering battery-1 SOC is 50 % and battery-2 is 20 % is presented in equation (20). The stability of the charger depends on the location of poles in the s-plane. Here the order of the system is five, representing the five number of poles. Therefore, the locations of the poles and zeros are extracted from the transfer function presented in (22). From the location, it is observed that all the poles and zeros lie on the left side of the s-plane, indicating that the charger is a stable and minimum phase system.

$$\left.\begin{array}{rl} P_1, P_2 & = (-1.0452 \pm 9.5627i) * 10^2 \\ Z_1, Z_2 & = (-0.1103 \pm 1.0129i) * 10^3 \\ P_3 & = (-2.5444 + 0.0000i) * 10^2 \\ Z_3, Z_4 & = (-0.0001 \pm 0.0000i) * 10^3 \\ P4 & = (-0.0008 + 0.0000i) * 10^2 \\ P5 & = (-0.0007 + 0.0000i) * 10^2 \end{array}\right\} \tag{22}$$

$$G_c(s) = 0.0013 + \frac{0.14031}{s} \tag{23}$$

$$\left.\begin{array}{rl} P_1, P_2 & = (-1.2111 \pm 9.4739i) * 10^2 \\ Z_1, Z_2 & = (-0.8255 \pm 9.0561i) * 10^2 \\ P_3 & = (-2.2815 + 0.0000i) * 10^2 \\ Z_3 & = (-0.0010 + 0.0000i) * 10^2 \\ P4 & = (-0.0011 + 0.0000i) * 10^2 \\ Z_4 & = (-0.0007 + 0.0000i) * 10^2 \\ P5 & = (-0.0007 + 0.0000i) * 10^2 \end{array}\right\} \tag{24}$$

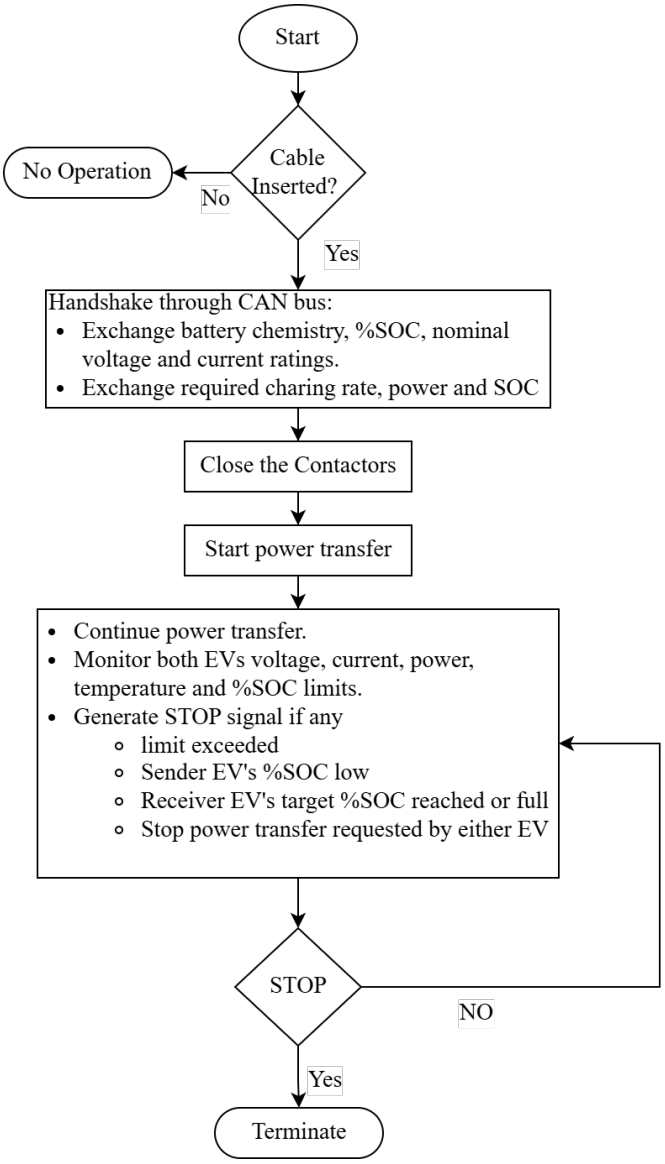

Fig. 7. Proposed charger control and communication flowchart .

To obtain the required response of the charger during dynamic conditions, a Proportional Integral (PI) controller is implemented. The difference between measured inductor current i_{L1} and reference inductor current i_{L1ref} is the error value that is sent to the PI controller to generate the regulated duty signal. The MATLAB Control System Designer tool is used to tune the PI controller to get the required charger performance. Hence, the proportional and integral gain values K_p= 0.0013, and K_i= 0.14031 are obtained. The controller transfer function is presented in (23).

The bode plot Fig. 9 (a) is drawn for the closed-loop transfer function considering battery-1 SOC is 50 % ($B_{1\_50\%}$), and battery-2 SOC level varied as 20 % ($B_{2\_20\%}$), 40 % ($B_{2\_40\%}$), and 70 % ($B_{2\_70\%}$).

Similarly, for the reverse buck mode of operation, the charger control to inductor current transfer function (21) is derived considering battery-2 SOC as 80 % and battery-1 as 10 %. All the poles and zeros are lies in the left half of s-

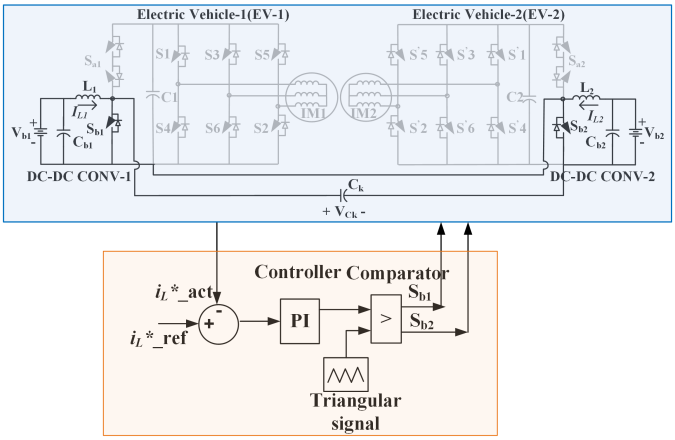

Fig. 8. Block diagram of proposed charger control scheme.

plane. The controller (23) is implemented to get the required dynamic behavior of the charger at 3C. Moreover, the charger performs satisfactorily during 1C and 2C discharging with the implementation of a controller.

The Fig. 9 (b) is drawn for the closed-loop transfer function considering battery-2 SOC as 80 % ($B_{2\_80\%}$), and battery-1 SOC level varied as 10 % ($B_{1\_10\%}$), 40 % ($B_{1\_40\%}$), and 60 % ($B_{1\_60\%}$). The charger control loop displays extremely consistent magnitude and phase characteristics across various battery SOC levels. The virtually overlapping bode graphs demonstrate the controller's excellent robustness by confirming that the plant dynamics are only slightly affected by variations in battery parameters. The system maintains enough phase margin, smooth high-frequency roll-off and proving stable and well-damped behavior under all operating conditions.

IV. Simulation Results

MATLAB/Simulink is used to model and simulate the proposed V2V charger for different charging modes such as forward boost, reverse buck, and forward buck-boost modes. Using equation (12), the inductor L_1, L_2 and capacitor C_k values for the proposed charger are computed. The battery specifications and design parameters of the charger for simulation study are provided in the TABLE I.

TABLE I
SPECIFICATIONS FOR SIMULATION AND EMULATION

Parameter	Value
Battery-1 Capacity (E_{b1})	40 kWh
Battery-2 Capacity (E_{b2})	100 kWh
Battery-1 Nominal Voltage (V_{b1})	350 V
Battery-2 Nominal Voltage (V_{b2})	450 V
Switching Frequency (f_{sw})	20 kHz
Filter Inductor (L_1)	0.5 mH
L_1 Internal Resistance (R_1)	0.005 Ω
Filter Inductor (L_2)	0.6 mH
L_2 Internal Resistance (R_2)	0.006 Ω
DC-link Capacitor (C_k)	1000 μF
DC-DC converter-1 Capacitor (C_{b1})	5.6 nF
DC-DC converter-2 Capacitor (C_{b2})	5.8 nF

$$\left.\begin{aligned}
\frac{di_{L1}(t)}{dt} &= \frac{v_{oc1}(t)}{L_1} - \frac{i_{L1}(t)(R_{L1}+R_{01})}{L_1} - \frac{v_{P1}(t)}{L_1} \\
\frac{di_{L2}(t)}{dt} &= -\frac{v_{ck}(t)}{L_2} + \frac{i_{L2}(t)(-R_{L2}-R_{ck}-R_{02})}{L_2} + \frac{v_{oc2}(t)}{L_2} - \frac{v_{p2}(t)}{L_2} \\
\frac{dv_{ck}(t)}{dt} &= \frac{i_{L2}(t)}{C_k} \\
\frac{dv_{p1}(t)}{dt} &= \frac{i_{L1}(t)}{C_{p1}} - \frac{v_{p1}(t)}{R_{p1}C_{p1}} \\
\frac{dv_{p2}(t)}{dt} &= \frac{i_{L2}(t)}{C_{p2}}\frac{v_{p2}(t)}{R_{p2}C_{p2}}
\end{aligned}\right\} \rightarrow dT_s \tag{13}$$

$$\left.\begin{aligned}
\frac{di_{L1}(t)}{dt} &= \frac{v_{oc1}(t)}{L_1} - \frac{i_{L1}(t)(R_{L1}+R_{01}+R_ck)}{L_1} - \frac{v_{ck}(t)}{L_1} - \frac{v_{P1}(t)}{L_1} \\
\frac{di_{L2}(t)}{dt} &= \frac{i_{L2}(t)(-(R_{L2}+R_{02}))}{L_2} + \frac{v_{oc2}(t)}{L_2} - \frac{v_{p2}(t)}{L_2} \\
\frac{dv_{ck}(t)}{dt} &= \frac{i_{L1}(t)}{C_k} \\
\frac{dv_{p1}(t)}{dt} &= \frac{i_{L1}(t)}{C_{p1}} - \frac{v_{p1}(t)}{R_{p1}C_{p1}} \\
\frac{dv_{p2}(t)}{dt} &= \frac{i_{L2}(t)}{C_{p2}}\frac{v_{p2}(t)}{R_{p2}C_{p2}}
\end{aligned}\right\} \rightarrow (1-d)T_s \tag{14}$$

$$\left.\begin{aligned}
\begin{bmatrix} \frac{di_{L1}(t)}{dt} \\ \frac{di_{L2}(t)}{dt} \\ \frac{dv_{ck}(t)}{dt} \\ \frac{dv_{p1}(t)}{dt} \\ \frac{dv_{p2}(t)}{dt} \end{bmatrix} &= \begin{bmatrix} \frac{-(R_{L1}+R_{01})}{L_1} & 0 & 0 & -\frac{1}{L1} & 0 \\ 0 & \frac{-R_{L2}-R_{02}-R_{ck}}{L2} & \frac{-1}{L_2} & 0 & -\frac{1}{L_2} \\ 0 & \frac{1}{C_k} & 0 & 0 & 0 \\ \frac{1}{Cp1} & 0 & 0 & -\frac{1}{R_{p1}C_{p1}} & 0 \\ 0 & \frac{1}{Cp2} & 0 & 0 & -\frac{1}{R_{p2}C_{p2}} \end{bmatrix} \begin{bmatrix} i_{L1}(t) \\ i_{L2}(t) \\ v_{ck}(t) \\ v_{p1}(t) \\ v_{p2}(t) \end{bmatrix} + \begin{bmatrix} \frac{1}{L_1} \\ 0 \\ 0 \\ 0 \\ 0 \end{bmatrix} v_{oc1}(t) + \begin{bmatrix} 0 \\ \frac{1}{L_2} \\ 0 \\ 0 \\ 0 \end{bmatrix} v_{oc2}(t) \\
v_0(t) &= \begin{bmatrix} 1 & 0 & 0 & 0 \end{bmatrix} \begin{bmatrix} i_{L1}(t) \\ i_{L2}(t) \\ v_{ck}(t) \\ v_{p1}(t) \\ v_{p2}(t) \end{bmatrix}
\end{aligned}\right\} \tag{15}$$

$$\left.\begin{aligned}
\begin{bmatrix} \frac{di_{L1}(t)}{dt} \\ \frac{di_{L2}(t)}{dt} \\ \frac{dv_{ck}(t)}{dt} \\ \frac{dv_{p1}(t)}{dt} \\ \frac{dv_{p2}(t)}{dt} \end{bmatrix} &= \begin{bmatrix} \frac{-(R_{L1}+R_{01}+R_{ck})}{L_1} & 0 & -\frac{1}{L1} & -\frac{1}{L1} & 0 \\ 0 & \frac{-R_{L2}-R_{02}}{L2} & 0 & 0 & -\frac{1}{L_2} \\ \frac{1}{C_k} & 0 & 0 & 0 & 0 \\ \frac{1}{Cp1} & 0 & 0 & -\frac{1}{R_{p1}C_{p1}} & 0 \\ 0 & \frac{1}{Cp2} & 0 & 0 & -\frac{1}{R_{p2}C_{p2}} \end{bmatrix} \begin{bmatrix} i_{L1}(t) \\ i_{L2}(t) \\ v_{ck}(t) \\ v_{p1}(t) \\ v_{p2}(t) \end{bmatrix} + \begin{bmatrix} \frac{1}{L_1} \\ 0 \\ 0 \\ 0 \\ 0 \end{bmatrix} v_{oc1}(t) + \begin{bmatrix} 0 \\ \frac{1}{L_2} \\ 0 \\ 0 \\ 0 \end{bmatrix} v_{oc2}(t) \\
v_0(t) &= \begin{bmatrix} 1 & 0 & 0 & 0 \end{bmatrix} \begin{bmatrix} i_{L1}(t) \\ i_{L2}(t) \\ v_{ck}(t) \\ v_{p1}(t) \\ v_{p2}(t) \end{bmatrix}
\end{aligned}\right\} \tag{16}$$

$$\left.\begin{bmatrix} \frac{d\hat{i}_{L1}(t)}{dt} \\ \frac{d\hat{i}_{L2}(t)}{dt} \\ \frac{d\hat{v}_{ck}(t)}{dt} \\ \frac{d\hat{v}_{p1}(t)}{dt} \\ \frac{d\hat{v}_{p2}(t)}{dt} \end{bmatrix} = \begin{bmatrix} \frac{-R_{L1}-R_{01}+R_{ck}(D-1)}{L_1} & 0 & \frac{D-1}{L1} & -\frac{1}{L1} & 0 \\ 0 & \frac{-R_{L2}-R_{02}-R_{ck}D}{L2} & \frac{-D}{L_2} & 0 & -\frac{1}{L_2} \\ \frac{1-D}{C_k} & \frac{D}{C_k} & 0 & 0 & 0 \\ \frac{1}{Cp1} & 0 & 0 & -\frac{1}{R_{p1}C_{p1}} & 0 \\ 0 & \frac{1}{Cp2} & 0 & 0 & -\frac{1}{R_{p2}C_{p2}} \end{bmatrix} \begin{bmatrix} \hat{i}_{L1}(t) \\ \hat{i}_{L2}(t) \\ \hat{v}_{ck}(t) \\ \hat{v}_{p1}(t) \\ \hat{v}_{p2}(t) \end{bmatrix} \right\} \tag{18}$$

$$+ \begin{bmatrix} \frac{R_{ck}}{L_1} & 0 & \frac{1}{L1} & 0 & 0 \\ 0 & \frac{-R_{ck}}{L2} & \frac{-1}{L_2} & 0 & 0 \\ \frac{-1}{C_k} & \frac{1}{C_k} & 0 & 0 & 0 \\ 0 & 0 & 0 & 0 & 0 \\ 0 & 0 & 0 & 0 & 0 \end{bmatrix} \begin{bmatrix} I_{L1} \\ I_{L2} \\ V_{ck} \\ V_{p1} \\ V_{p2} \end{bmatrix} \hat{d}(t) + \begin{bmatrix} \frac{1}{L_1} \\ 0 \\ 0 \\ 0 \\ 0 \end{bmatrix} \hat{v}_{oc1}(t) + \begin{bmatrix} 0 \\ \frac{1}{L_2} \\ 0 \\ 0 \\ 0 \end{bmatrix} \hat{v}_{oc2}(t)$$

$$\frac{\hat{i}_{L1}(s)}{\hat{d}(s)} = \frac{1.715 * 10^6 s^4 + 3.785 * 10^8 s^3 + 1.78 * 10^{12} s^2 + 2.623 * 10^{11} s + 9.502 * 10^9}{s^5 + 463.6 s^4 + 9.786 * 10^5 s^3 + 2.356 * 10^8 s^2 + 3.592 * 10^7 s + 1.353 * 10^6} \tag{20}$$

$$\frac{\hat{i}_{L2}(s)}{\hat{d}(s)} = \frac{1.735 * 10^6 s^4 + 2.867 * 10^8 s^3 + 1.434 * 10^{12} s^2 + 2.497 * 10^{11} s + 1.047 * 10^{10}}{s^5 + 470.5 s^4 + 9.676 * 10^5 s^3 + 2.083 * 10^8 s^2 + 3.782 * 10^7 s + 1.647 * 10^6} \tag{21}$$

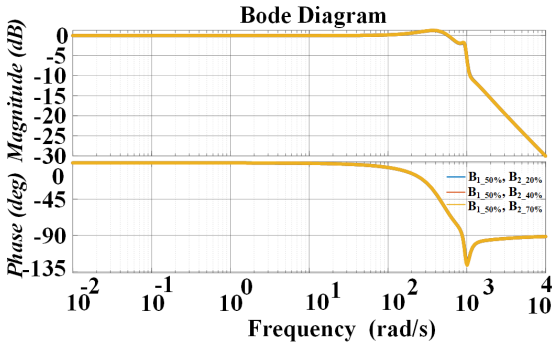

(a)

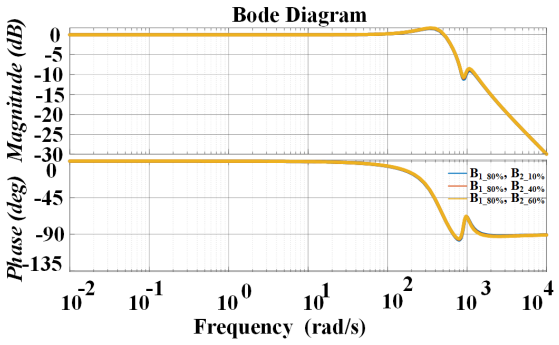

(b)

Fig. 9. Closed loop bode plot of the proposed charger (a) Forward boost mode of operation, (b) Reverse buck mode of operation.

A. Forward Boost Mode of Operation:

In this configuration, EV-1 functions as a sender and EV-2 as a receiver with V_{b1} as 350 V, and V_{b2} as 450 V. In order to transmit energy between the vehicles, the control algorithm is implemented by assuming the sender vehicle inductor current (i.e.,I_{L1}) as a reference. To verify the proposed V2V charger performance at different charging speeds, different inductor current references are taken based on the charging/discharging current rates of the battery, such as 1C, 2C, and 3C (The nominal current rating of a battery is known as the battery's 1C rating). As charging and discharging rates increase, the speed of charging and discharging increases. The simulation results of the forward boost mode of operation are depicted in Fig. 10. At 0.3 s, the inductor current reference I_{L1} is stepped from 100 A to 200 A; during this change, the V_{b1} voltage reduces from 375 V to 371 V, and V_{b2} increases from 486 V to 487.5 V. At 0.55 s the inductor current reference I_{L1} is stepped from 200 A to 300 A; during this change the V_{b1} voltage reduces from 371 V to 368 V and V_{b2} increases from 487.5 V to 489 V. Here, I_{L1} varies as multiples of the battery C-rating (1C, 2C, and 3C). The positive value of battery current indicates that it is getting discharged and similarly the negative battery current indicates that it is getting charged. From the Fig. 10, it is observed that as the battery-1 discharging current magnitude and duration increases its SOC is getting decreased. On the other side battery-2 current is negative, that means it is getting charged and its SOC is increasing with the magnitude of current and duration.

B. Reverse Buck Mode of Operation:

In this configuration, voltage V_{b1} is 350 V, and voltage V_{b2} is 450 V. At 0.3 s, the inductor current reference I_{L2} is stepped from 100 A to 200 A; during this change, the V_{b2} voltage reduces from 482 V to 480 V, and V_{b1} increases from 382 V to 385. At 0.55 s the inductor current reference I_{L2} is stepped from 200 A to 300 A; during this change the V_{b2} voltage

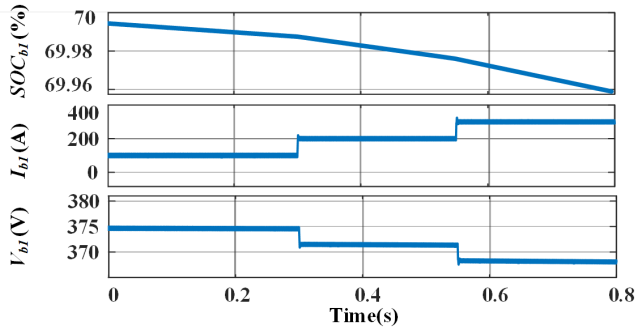

(a)

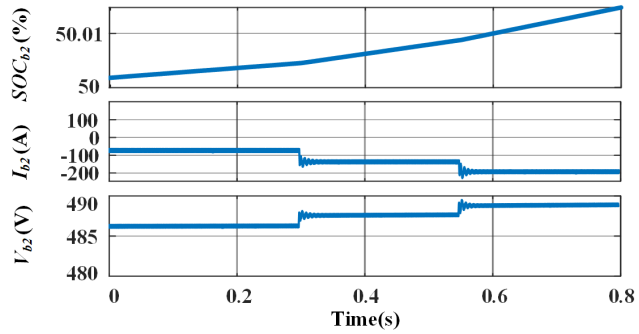

(b)

Fig. 10. Simulation results of the V2V charger during forward boost mode of operation (a) Battery-1 SOC, voltage, and current, (b) Battery-2 SOC, voltage, and current.

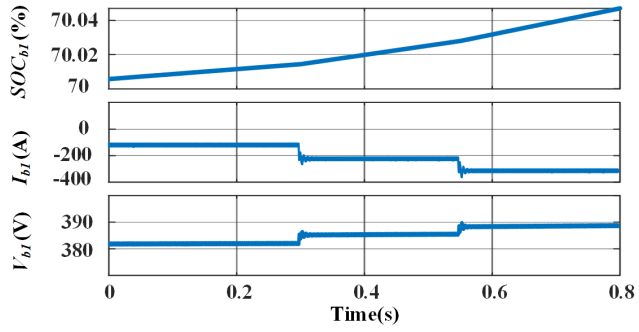

(a)

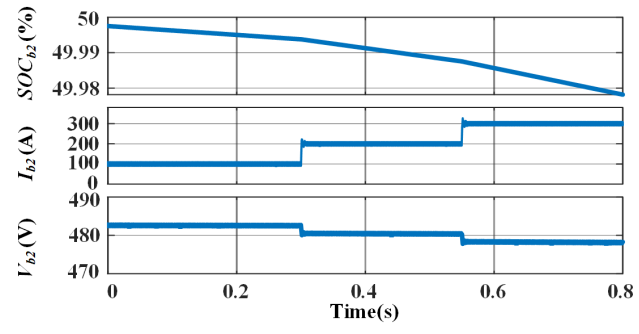

(b)

Fig. 11. Simulation results of the V2V charger during reverse buck mode of operation (a) Battery-1 SOC, voltage, and current, (b) Battery-2 SOC, voltage, and current.

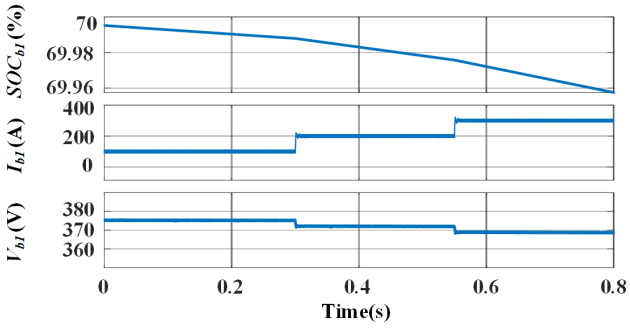

(a)

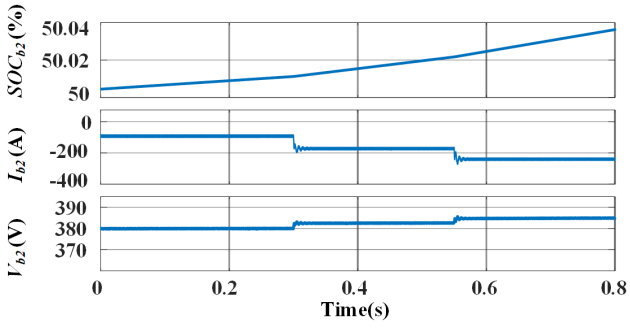

(b)

Fig. 12. Simulation results of the V2V charger during forward buck-boost mode of operation (a) Battery-1 SOC, voltage, and current, (b) Battery-2 SOC, voltage, and current.

reduces from 480 V to 378 V and V_{b1} increases from 385 V to 389 V. Here, I_{L2} varies as multiples of the battery C-rating (1C, 2C, and 3C). From the Fig. 11, it is observed that as the battery-2 discharging current increases, its SOC is getting decreased as duration increases. On the other side battery-1 current is negative, that means it is getting charged and its SOC is increases with the magnitude of current and duration.

C. Forward Buck-Boost Mode of Operation:

In this configuration, batteries are considered with equal voltage of 350 V and different SOC levels. At 0.3 s, the inductor current reference I_{L1} is stepped from 100 A to 200 A; during this change, the V_{b1} voltage reduces from 375 V to 371 V, and V_{b2} increases from 380 V to 482 V. At 0.55 s the inductor current reference I_{L1} is stepped from 200 A to 300 A; during this change the V_{b1} voltage reduces from 371 V to 369 V and V_{b2} increases from 482 V to 485 V. Here, I_{L1} varies as multiples of the battery C-rating (1C, 2C, and 3C). From Fig. 12, it is observed that battery-1 is getting discharged and, on the other side battery-2 is charged.

D. Performance Evaluation and Comparison Study:

The proposed charger's working efficiency and its performance are evaluated by quantifying the various losses such as switching losses of the switches (Switches_swi), conduction losses of the switches (Switches_cond) and conduction losses of the passive components (Passive_cond) using thermal model in PSIM software. For the output power of 10 kW, 15 kW, and

TABLE II
COMPARISON OF DIFFERENT V2V CHARGERS

Parameter	[16]	[19]	[25]	[26]	[27]	[29]	[30]	Proposed
Switches	4	8	6	16	12	12	8	2
Diodes	4	8	6	16	12	12	8	2
Inductors	2	2	3	2	6	4	2	2
Capacitors	2	4	2	4	2	6	4	3
Total Components	12	22	17	38	32	34	22	9
Use of motor winding	No	No	No	Yes	Yes	No	No	No
Switching frequency (kHz)	200	50	10	20	3.1	20	20	20
Power conversion steps	2	2	1	2	1	4	2	1
Bi-directional Power flow	No	Yes	Yes	Yes	No	Yes	Yes	Yes
Buck operation	No	Yes	Yes	Yes	Yes	No	Yes	Yes
Boost operation	Yes	Yes	Yes	Yes	No	No	Yes	Yes
Buck-boost operation	Yes	Yes	Yes	No	No	Yes	Yes	Yes
Direct/Indirect V2V Transfer	Direct	Indirect	Direct	Direct	Direct	Indirect	Direct	Direct
Switching losses (kW)	NA	NA	NA	4.1	NA	2.284	0.2	0.514
Conduction losses (kW)	NA	NA	NA	3.4	NA	0.56	0.203	0.185
Motor winding losses (kW)	No	NA	NA	4.45	NA	NA	NA	NA
Output power (kW)	3	NA	75	130	1.5	19.4	19.4	20
Peak Efficiency (%)	NA	NA	96.7	91.5	99.47	85.34	97.92	96.6

20 kW, the various losses of the charger during the forward boost mode, reverse buck mode, and forward buck-boost mode of operation are presented in Fig. 13. The overall efficiency curves of the charger during all mode of operations at different power levels are depicted in Fig. 14. From the graph, it can be noticed that proposed V2V charger exhibits a maximum efficiencies of 97.12 %, 97.1 % and 97 % at the 10 kW output power during forward boost, reverse buck and forward buck-boost modes operations respectively.

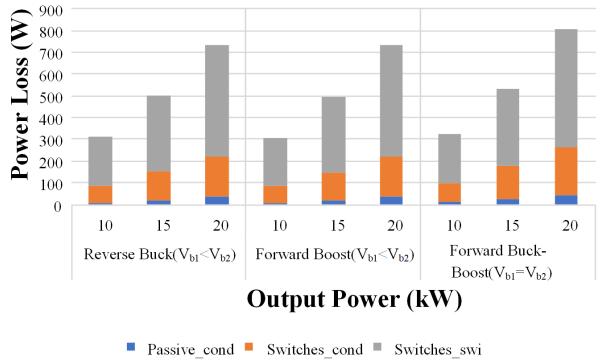

Fig. 13. Power loss vs Output power.

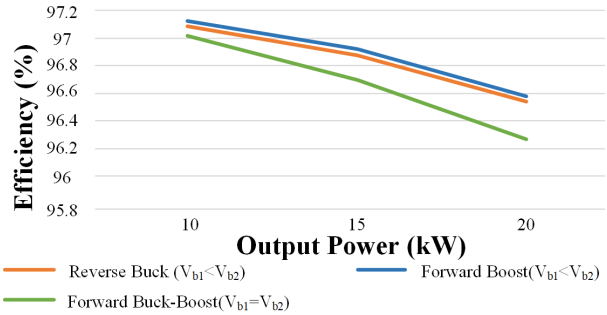

Fig. 14. Efficiency vs Output power.

The proposed V2V charger performance is evaluated by comparing with the various parameters of the existing V2V chargers [16], [19], [25]–[27], [29], [30] like components count, utilization of motor windings, power conversion steps, number of switches in conduction and efficiency. The comparison study is presented in the TABLE II. The charger in [26], [29], [30] and the proposed charger work at a switching frequency of 20 kHz, and the components count, such as switches, inductors and capacitors in the proposed charger, is extremely low. This contributes to a compact size of charger, which is beneficial in the automobile industry because of space constraints. The number of power conversion steps for the proposed charger is one, whereas chargers in [29] it is four and in [16], [19], [26], [30] it is two. As the EV motors are not involved in the power transfer between the vehicle, various losses associated with the motors get eliminated in the proposed, [16], [29] and [30] chargers. The proposed converter, [29] and [30] are reported respective efficiencies of 96.6 %, 85.34 % and 97.92 % at 20 kW output power. The efficiency of proposed V2V charger is evaluated by conducting thermal modeling in PSIM, whereas the [30] evaluated using theoretical calculation and ignored thermal effects. Hence, results in the slight difference in the efficiencies. From the TABLE II, it can be noticed that proposed converter provides 25 % to 76.3 % of total component reduction compared to the [16] and [26].

V. EXPERIMENTAL RESULTS

A. Low Power Proof-of-Concept:

To confirm the proposed V2V charger's desired performance, a proof-of-concept is developed as depicted in Fig. 15. Its specifications are listed in TABLE III. The control pulses needed for the charger are produced by the TMS320F28379D digital signal processor.

The proposed V2V charger experimental waveforms during the forward boost mode of operation with the battery voltage of V_{b1} as 12 V and V_{b2} as 25.6 V are presented in Fig. 16. The waveforms of both vehicles battery voltages V_{b1}, V_{b2},

TABLE III
HARDWARE SETUP PARAMETERS

Parameter	Value
Battery-1 Capacity (E_{b1})	120 Wh
Battery-2 Capacity (E_{b2})	307 Wh
Battery-1 Nominal Voltage (V_{b1})	12 V
Battery-2 Nominal Voltage (V_{b2})	25.6 V
Switching Frequency (f_{sw})	20 kHz
Filter Inductor (L_1)	1 mH
Filter Inductor (L_2)	1 mH
Dc-link Capacitor (C_k)	1000 μF
Mosfet Switch(IRFP150N)	100 V/42 A
Driver IC	HCPL A3120

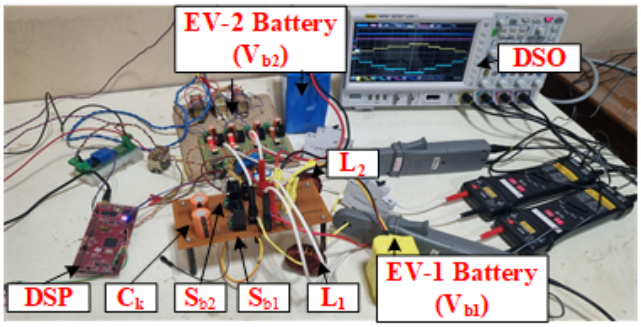

Fig. 15. Experimental setup of the proposed V2V charger.

and inductor currents I_{L1}, I_{L2} are shown in Fig. 16(a), during 1C discharge current rate of EV-1 (i.e., I_{b1} = I_{L1} = 10 A). The voltages V_{Sb1}, V_{Sb2}, and currents I_{Sb1}, I_{Sb2} of switches Sb_1, Sb_2, the firing pulse $pulse_{Sb1}$, and capacitor voltage V_{Ck} waveforms are shown in Fig. 16(b). The dynamic performance of the charger analyzed at 0.25C, 0.5C, 0.75C, and 1C discharging current rates EV-1 and corresponding waveforms of battery-1, 2 voltages V_{b1}, V_{b2}, and inductor currents I_{L1} and I_{L2} are shown in Fig. 16(d).

During the reverse buck mode of operation, the experimental waveforms are presented in Fig. 17, with the battery voltage of V_{b1} as 12 V and V_{b2} as 25.6 V. The waveforms of both vehicles battery voltages V_{b1}, V_{b2}, and inductor currents I_{L1} and I_{L2} are shown in Fig. 17(a), during 1C charge current rate of EV-1 (i.e., I_{b1} = I_{L1} = -10 A). The voltages V_{Sb1}, V_{Sb2}, and currents I_{Sb1}, I_{Sb2} of switches Sb_1, Sb_2, firing pulse $Pulse_{Sb1}$, and capacitor voltage V_{Ck} waveforms are shown in Fig. 17(b). The dynamic performance of the charger analyzed at 0.25C, 0.5C, 0.75C, and 1C charging current rates of EV-1 and corresponding waveforms of battery-1, 2 voltages V_{b1}, V_{b2}, and inductor currents I_{L1} and I_{L2} are shown in Fig. 17(d).

In a similar manner, the charger's functionality in forward buck-boost mode of operation is tested with the batteries voltage of 12 V ($V_{b1} = V_{b2}$) for both vehicles. The corresponding waveforms of battery-1, 2 voltage V_{b1}, V_{b2}, inductors current I_{L1}, I_{L2}, switches voltage V_{Sb1}, V_{Sb2}, current I_{Sb1}, I_{Sb2}, firing pulse $Pulse_{Sb1}$, and capacitor voltage V_{Ck} are shown in Fig. 18, at 0.25C, 0.5C, 0.75C, and 1C discharging current rates of battery-1 of EV-1.

The Fig. 19 depicts the bi-directional operation of the proposed charger. In Fig. 19(a), from t_0 to t_1 s, the power is flowing from EV-2 to EV-1 with V_{b1} as 12 V and V_{b2} as 25.6 V, indicating that EV-2 is discharging and its current I_{L2} is positive, and EV-1 is charging and its current I_{L1} is negative.

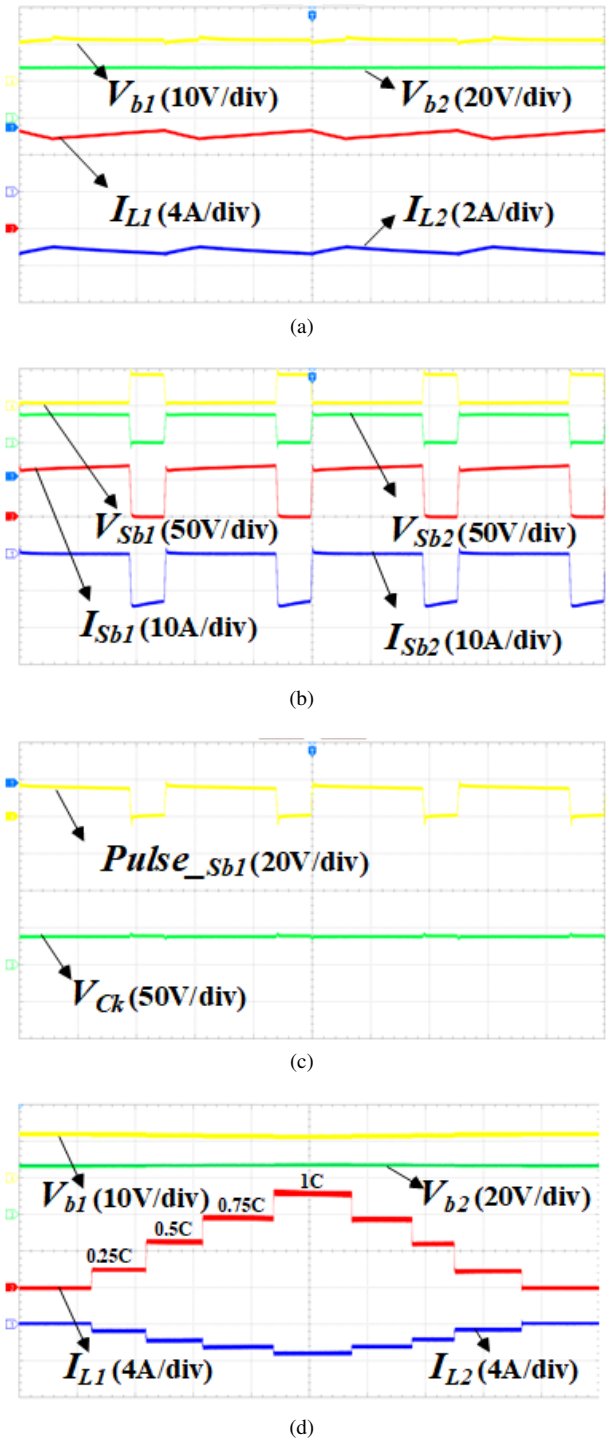

Fig. 16. Experimental wave forms of the proposed V2V charger during forward boost mode of operation (a) V_{b1}, V_{b2}, I_{L1} and I_{L2} during 1C discharging rate (i.e., Battery-1 discharging at a current of 10 A), (b) V_{Sb1}, V_{Sb2}, I_{Sb1} and I_{Sb2} are switch voltages and currents, (c) $pulse_{Sb1}$, V_{Ck} are switch firing pulse and capacitor voltage, (d) V_{b1}, V_{b2}, I_{L1} and I_{L2} during 0.25C, 0.5C, 0.75C, and 1C discharging current rate.

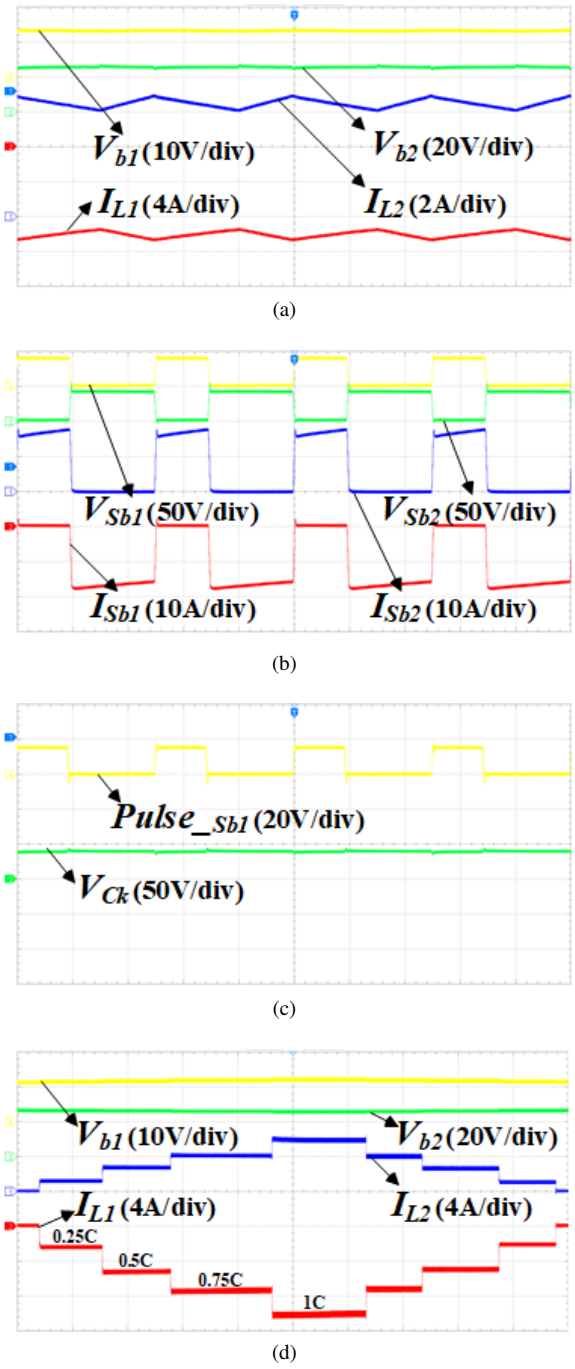

Fig. 17. Experimental wave forms of the proposed V2V charger during reverse buck mode of operation: (a) V_{b1}, V_{b2}, I_{L1} and I_{L2} during 1C charging rate (i.e., Battery-1 charging at a current of 10 A). (b) V_{Sb1}, V_{Sb2}, I_{Sb1} and I_{Sb2} are switch voltages and currents. (c) $pulse_{Sb1}$, V_{Ck} are switch firing pulse and capacitor voltage. (d) V_{b1}, V_{b2}, I_{L1} and I_{L2} during 0.25C, 0.5C, 0.75C, and 1C charging current rate.

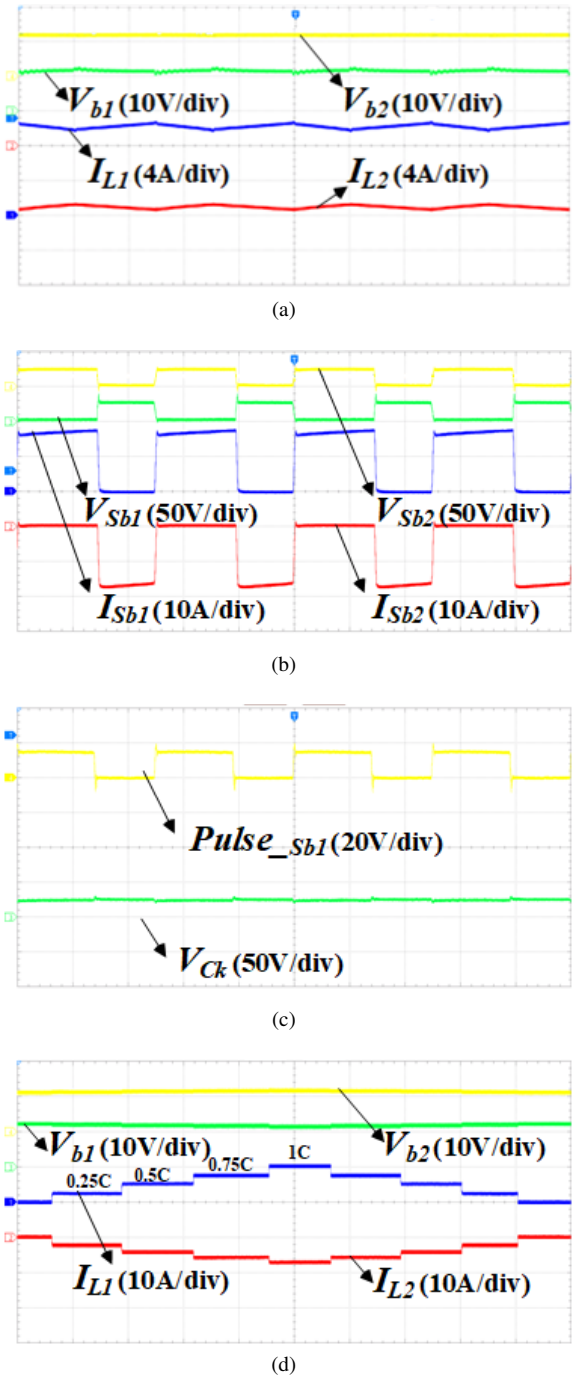

Fig. 18. Experimental wave forms of the proposed V2V charger during forward buck-boost mode of operation (a) V_{b1}, V_{b2}, I_{L1} and I_{L2} during 1C discharging rate (i.e., Battery-1 discharging at a current of 10 A), (b) V_{Sb1}, V_{Sb2}, I_{Sb1} and I_{Sb2} are switch voltages and currents, (c) $pulse_{Sb1}$, V_{Ck} are switch firing pulse and capacitor voltage, (d) V_{b1}, V_{b2}, I_{L1} and I_{L2} during 0.25C, 0.5C, 0.75C,and 1C discharging current rate.

Between t_0 and t_1 s, the mode of operation is the reverse buck mode of operation. From t_1 to t_2 s, the power is flowing from EV-1 to EV-2, indicating that EV-2 is charging and its current I_{L2} is negative, and EV-1 is discharging and its current I_{L1} is positive. Between t_1 and t_2 s, the mode of operation is forward boost mode of operation. Following t_2 s, the power is flowing from EV-2 to EV-1, indicating the reverse buck mode of operation.

Fig. 19(b) represents the bi-directional power flow with V_{b1} as 12 V and V_{b2} as 12 V. Here, from t_0 to t_1 s, the power is flowing from EV-2 to EV-1, indicating that EV-2 is discharging and its current I_{L2} is positive, and EV-1 is charging and its current I_{L1} is negative. From t_1 to t_2 s, the power is flowing

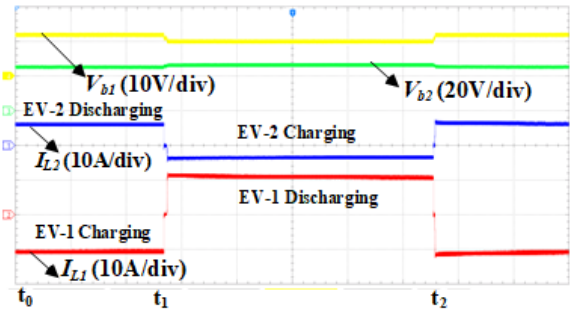

(a)

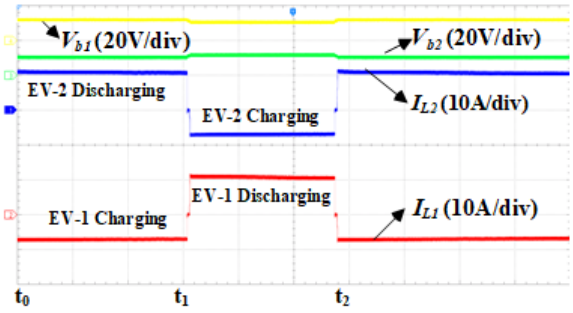

(b)

Fig. 19. Experimental waveforms of the bi-directional operation of the proposed V2V charger (a) Forward boost to Reverse buck and vice-versa V_{b1} as 12 V and V_{b2} as 25.6 V, (b) Forward buck-boost to Reverse buck-boost and vice-versa V_{b1} as 12 V and V_{b2} as 12 V.

from EV-1 to EV-2, indicating that EV-2 is charging and its current I_{L2} is negative, and EV-1 is discharging and its current I_{L1} is positive. Following t_1 s, the power is flowing from EV-2 to EV-1, indicating. In this case battery ratings are equal, and the mode of operation is called forward buck-boost mode of operation.

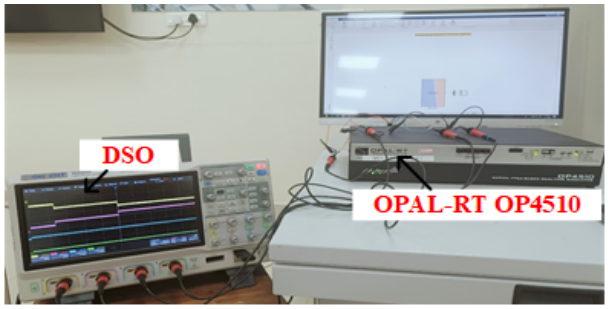

Fig. 20. Experimental setup of the proposed V2V charger.

B. OPAL-RT Experimentation:

To further test the proposed V2V chargers' real time behavior with actual EV battery voltages, an OPAL-RT emulation study is conducted. The experimental setup of the OPAL-RT emulation along with the oscilloscope is depicted in the Fig. 20. The specifications presented in TABLE I are considered for the emulation.

The OPAL-RT experimental results for the forward boost mode of operation with V_{b1} as 350 V and V_{b2} as 450 V are

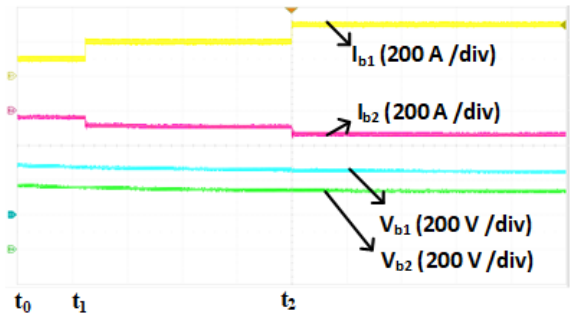

(a)

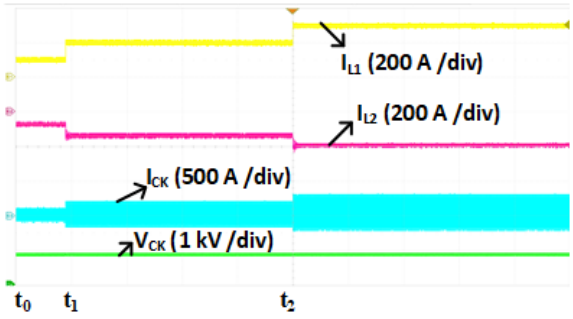

(b)

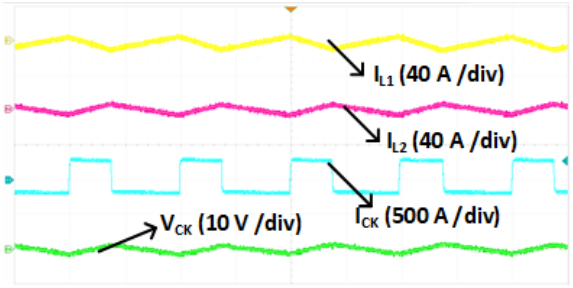

(c)

Fig. 21. Experimentation results during forward boost mode of operation (a) V_{b1}, V_{b2}, I_{b1} and I_{b2}, (b) I_{L1}, I_{b2} I_{CK} and V_{CK}, (c) ripple waveforms I_{L1}, I_{b2} I_{CK} and V_{CK} during 3C discharging.

depicted in Fig. 21. The waveforms of V_{b1}, V_{b2}, I_{b1} and I_{b2} are presented in the Fig. 21(a). The I_{L1}, I_{L2}, I_{CK} and V_{CK} waveforms are depicted in the Fig. 21(b). In the figure from t_0 to t_1 s the I_{L1} average value is 100 A, from t_1 to t_2 s is 200 A, and after t_2 s it is 300 A, which are multiples of to the battery C-rating. The positive value of battery current indicates that it is getting discharged and similarly the negative battery current indicates that it is getting charged. The ripple waveforms of I_{L1}, I_{L2} I_{CK} and V_{CK} after t_2 during 3C discharging are presented in Fig. 21(c). From the ripple waveforms, the ripple values of I_{L1} and I_{L2} and V_{CK} are 20.5 A, 17 A and 6.13 V respectively, which are with in the limit of designed values. The OPAL-RT experimental results for the reverse buck mode of operation with V_{b1} as 350 V and V_{b2} as 450 V are depicted in Fig. 22. The waveforms of V_{b1}, V_{b2}, I_{b1} and I_{b2} are presented in the Fig. 22(a). The I_{L1}, I_{L2}, I_{CK} and V_{CK} waveforms are depicted in the Fig. 22(b). In the figure from t_0 to t_1 s the I_{L2} average value is 100 A, from t_1 to t_2 s is 200 A, and after t_2 s it is 300 A, which are multiples of to the

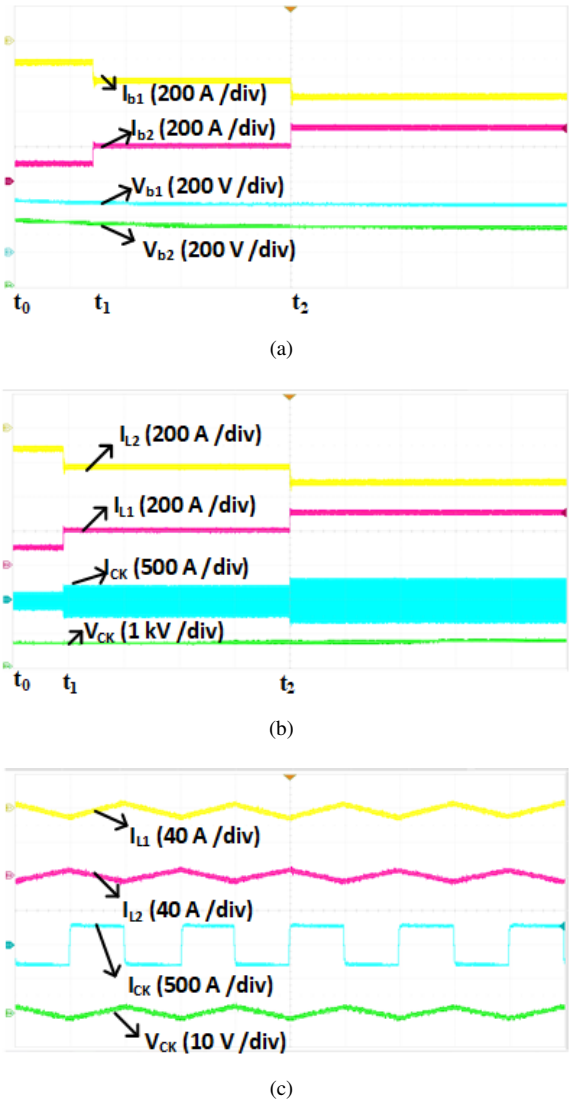

Fig. 22. Experimentation results during reverse buck mode of operation (a) V_{b1}, V_{b2}, I_{b1} and I_{b2}, (b) I_{L1}, I_{b2} I_{CK} and V_{CK}, (c) ripple waveforms I_{L1}, I_{b2} I_{CK} and V_{CK} during 3C discharging.

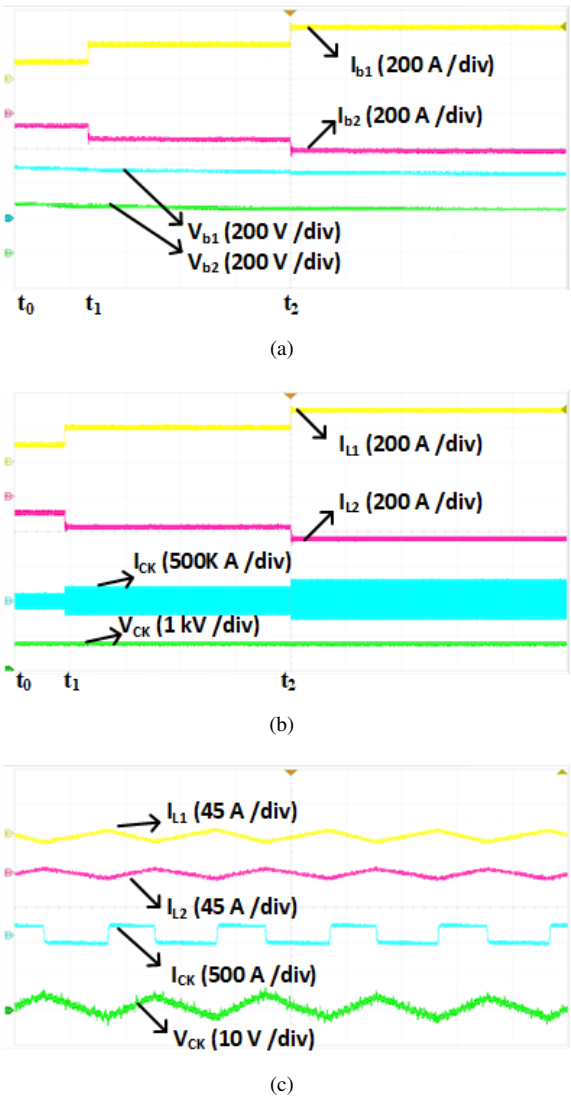

Fig. 23. Experimentation results during forward buck-boost mode of operation (a) V_{b1}, V_{b2}, I_{b1} and I_{b2}, (b) I_{L1}, I_{b2} I_{CK} and V_{CK}, (c) ripple waveforms I_{L1}, I_{b2} I_{CK} and V_{CK} during 3C discharging.

battery C-rating. The positive value of I_{b2} and negative value of I_{b1} confirms the reverse buck operation and energy transfer from the EV-2 to EV-1. The ripple waveforms of I_{L1}, I_{L2} I_{CK} and V_{CK} after t_2 during 3C discharging are presented in Fig. 22(c). From the ripple waveforms, the ripple values of I_{L1} and I_{L2} and V_{CK} are 21 A, 18 A and 7.9 V respectively, which are with in the limit of designed values.

The OPAL-RT experimental results for the forward buck-boost mode of operation with V_{b1} as 350 V and V_{b2} as 350 V are depicted in Fig. 23. The waveforms of V_{b1}, V_{b2}, I_{b1} and I_{b2} are presented in the Fig. 23(a). The I_{L1}, I_{L2}, I_{CK} and V_{CK} waveforms are depicted in Fig. 23(b). In the figure from t_0 to t_1 s the I_{L1} average value is 100 A, from t_1 to t_2 s is 200 A, and after t_2 s it is 300 A, which are multiples of the battery C-rating. The positive value of I_{b1} and negative value of I_{b2} confirm the forward buck-boost operation and energy transfer from the EV-1 to EV-2. The ripple waveforms I_{L1}, I_{L2}, I_{CK} and V_{CK} after t_2 during 3C discharging are presented in Fig. 23(c). From the ripple waveforms, the ripple values of I_{L1} and I_{L2} and V_{CK} are 18 A, 15 A and 7 V respectively, which are within the limit of designed values.

From the above OPAL-RT experimental results, the proposed V2V charger real-time response with the proposed controller is verified for all the modes of operation under different charging rates.

VI. Conclusion

In this paper, a new V2V charger is presented to share energy between two EVs. The electrical power between the two EVs is transferred with the help of capacitor coupling and a DC-DC converter from each EV. Unlike other V2V charging configurations, this work neither requires motor windings nor the inverter circuit of the EVs. The analytical waveforms illustrating the proposed charger's behavior in all operating modes are presented. The small-signal modeling of the charger is described, and the controller performance is investigated

under different battery SOC levels and internal parameter modifications. The associated bode charts indicate the robust behavior of the controller. The bidirectional power transfer in real-time with EV battery voltages of 350 V and 450 V is verified in forward boost, reverse buck and forward buck-boost modes of operation using MATLAB/Simulink. Additionally, the power loss calculation and efficiency of the presented V2V charger are evaluated using PSIM thermal modeling for 20 kW output power. The charger achieved an efficiency of 96.57 % in the forward boost mode, 96.56 % in the reverse buck mode, and 96.26 % in the forward buck–boost mode of operation. Additionally, it provides an 25 % to 76 % reduction in component count compared to existing topologies. Further, a low-power laboratory prototype for proof of concept is developed with EV battery voltages of 12 V and 25.6 V. Its experimental results in all the operating modes and for the charging rates of 0.25C, 0.5C, 0.75C and 1C are presented. In addition, bi-directional power flow from one mode to another is demonstrated and the respective waveforms are presented. To prove the proposed charger and its controller's real-time applicability, OPAL-RT experimentation was conducted with real-world EV specifications and the respective results in all modes of operation are presented. From the results it is evident that the bi-directional power flow in both static and dynamic conditions is operational.

REFERENCES

[1] H. H. Kore and S. Koul, "Electric vehicle charging infrastructure: positioning in India," Management of Environmental Quality: An International Journal, vol. ahead-of-print, no. ahead-of-print, Feb. 2022, doi: https://doi.org/10.1108/meq-10-2021-0234.

[2] A. Ghosh, "Possibilities and Challenges for the Inclusion of the Electric Vehicle (EV) to Reduce the Carbon Footprint in the Transport Sector: A Review," Energies, vol. 13, no. 10, p. 2602, May 2020, doi: https://doi.org/10.3390/en13102602.

[3] B. V. Kumar and A. F. M A, "A Review of Technical Impact of Electrical Vehicle Charging Stations on Distribution Grid," 2023 International Conference on Recent Advances in Electrical, Electronics & Digital Healthcare Technologies (REEDCON), pp. 559–564, May 2023, doi: https://doi.org/10.1109/reedcon57544.2023.10150680.

[4] M. R. Khalid, I. A. Khan, S. Hameed, M. S. J. Asghar, and J.-S. Ro, "A Comprehensive Review on Structural Topologies, Power Levels, Energy Storage Systems, and Standards for Electric Vehicle Charging Stations and Their Impacts on Grid," IEEE Access, vol. 9, pp. 128069–128094, 2021, doi: https://doi.org/10.1109/ACCESS.2021.3112189.

[5] A. G. Boulanger, A. C. Chu, S. Maxx, and D. L. Waltz, "Vehicle Electrification: Status and Issues," Proceedings of the IEEE, vol. 99, no. 6, pp. 1116–1138, Jun. 2011, doi: https://doi.org/10.1109/jproc.2011.2112750.

[6] S. Haghbin, S. Lundmark, M. Alakula, and O. Carlson, "Grid-Connected Integrated Battery Chargers in Vehicle Applications: Review and New Solution," IEEE Transactions on Industrial Electronics, vol. 60, no. 2, pp. 459–473, Feb. 2013, doi: https://doi.org/10.1109/tie.2012.2187414.

[7] S. Das, P. Acharjee, and A. Bhattacharya, "Charging Scheduling of Electric Vehicle incorporating Grid-to-Vehicle (G2V) and Vehicle-to-Grid (V2G) technology considering in Smart-Grid," IEEE Transactions on Industry Applications, pp. 1–1, 2020, doi: https://doi.org/10.1109/tia.2020.3041808.

[8] K. M.Tan, V.K.Ramachandaramurthy, and J.Y.Yong, "Bidirectional battery charger for electric vehicle," 2014 IEEE Innovative Smart Grid Technologies - Asia (ISGT ASIA), May 2014, doi: https://doi.org/10.1109/isgt-asia.2014.6873826.

[9] E. Martinez-Vera and P. B. Sanchez, "Review of Bidirectional DC-DC Converters and Trends in Control Techniques for Applications in Electric Vehicles," IEEE Latin America Transactions, vol. 22, no. 2, pp. 144–155, Jan. 2024, doi: https://doi.org/10.1109/TLA.2024.10412031.

[10] S. S. Sayed and A. M. Massoud, "Review on State-of-the-Art Unidirectional Non-Isolated Power Factor Correction Converters for Short-/Long-Distance Electric Vehicles," IEEE Access, vol. 10, pp. 11308–11340, 2022, doi: https://doi.org/10.1109/access.2022.3146410.

[11] V. M. Iyer, S. Gulur, G. Gohil, and S. Bhattacharya, "An Approach Towards Extreme Fast Charging Station Power Delivery for Electric Vehicles with Partial Power Processing," IEEE Transactions on Industrial Electronics, vol. 67, no. 10, pp. 8076–8087, Oct. 2020, doi: https://doi.org/10.1109/tie.2019.2945264.

[12] J. Anzola, I. Aizpuru, and A. Arruti, "Partial Power Processing Based Converter for Electric Vehicle Fast Charging Stations," Electronics, vol. 10, no. 3, p. 260, Jan. 2021, doi: https://doi.org/10.3390/electronics10030260.

[13] Radha Kushwaha, Vinod Khadkikar, and Bashar Zahawi, "11 kW Integrated On-Board Fast Charger Using Partial Power Conversion," IEEE Industry Applications Society Annual Meeting (IAS), pp. 1–6, Oct. 2024, doi: https://doi.org/10.1109/ias55788.2024.11023797.

[14] Radha Kushwaha, Vinod Khadkikar, S. Singh, H. H. Zeineldin, Rabeb Mizouni, and Hadi Otrok, "An Efficient Three-Port Partial Power Converter based EV On-board Fast Charger," IEEE International Conference on Power Electronics, Drives and Energy Systems (PEDES), pp. 1–6, Dec. 2022, doi: https://doi.org/10.1109/pedes56012.2022.10080032.

[15] Tiago, L. Machado, D. Pedrosa, C. Martins, and J. L. Afonso, "Comparative Analysis of Vehicle-to-Vehicle (V2V) Power Transfer Configurations without Additional Power Converters," IEEE 14th International Conference on Compatibility, Power Electronics and Power Engineering (CPE-POWERENG), pp. 88–93, Jul. 2020, doi: https://doi.org/10.1109/CPE-POWERENG48600.2020.9161697.

[16] T. Sousa, V. Monteiro, J. O. Fernandes, C. Couto, A. A. Nogueiras, and J. L. Afonso, "New Perspectives for Vehicle-to-Vehicle (V2V) Power Transfer," Conference of the Industrial Electronics Society, Oct. 2018, doi: https://doi.org/10.1109/iecon.2018.8591209.

[17] M. A. Masrur et al., "Military-Based Vehicle-to-Grid and Vehicle-to-Vehicle Microgrid—System Architecture and Implementation," IEEE Transactions on Transportation Electrification, vol. 4, no. 1, pp. 157–171, Mar. 2018, doi: https://doi.org/10.1109/tte.2017.2779268.

[18] G. Li, L. Boukhatem, L. Zhao and J. Wu, "Direct Vehicle-to-Vehicle Charging Strategy in Vehicular Ad-Hoc Networks," 2018 9th IFIP International Conference on New Technologies, Mobility and Security (NTMS), Paris, France, 2018, pp. 1-5, doi: 10.1109/NTMS.2018.8328689.

[19] T. J. C. Sousa, V. Monteiro, S. Coelho, L. Machado, D. Pedrosa, and J. L. Afonso, "Electric Vehicle Battery Charging Station based on Bipolar dc Power Grid with Grid-to-Vehicle, Vehicle-to-Grid and Vehicle-to-Vehicle Capabilities," EAI Endorsed Transactions on Energy Web, vol. 9, no. 5, p. e5, Feb. 2023, doi: https://doi.org/10.4108/ew.v9i5.3049.

[20] A. Namadmalan, K. Rouzbehi, J. M. Escaño, and C. Bordons, "Dual-Active Bridge Series Resonant Electric Vehicle Charger: A Self-Tuning Method," Electronics, vol. 9, no. 2, p. 253, Feb. 2020, doi: https://doi.org/10.3390/electronics9020253.

[21] S. S. Trivedi and A. V. Sant, "Comparative analysis of dual active bridge dc–dc converter employing Si, SiC and GaN MOSFETs for G2V and V2G operation," Energy Reports, vol. 8, pp. 1011–1019, Nov. 2022, doi: https://doi.org/10.1016/j.egyr.2022.08.100.

[22] N. D. Dao, D.-C. Lee, and Q. D. Phan, "High-Efficiency SiC-Based Isolated Three-Port DC/DC Converters for Hybrid Charging Stations," IEEE Transactions on Power Electronics, vol. 35, no. 10, pp. 10455–10465, Oct. 2020, doi: https://doi.org/10.1109/tpel.2020.2975124.

[23] Md Safayatullah, Reza Rezaii, Fahad Alaq, and I. Batarseh, "A Three-Port DC-DC-DC Converter based on Dual Active Bridge Series Resonant Topology for Electric Vehicle DC Fast Charging Applications," 2022 IEEE Energy Conversion Congress and Exposition (ECCE), pp. 1–7, Oct. 2022, doi: https://doi.org/10.1109/ecce50734.2022.9947971.

[24] G. R. Chandra Mouli, J. Schijffelen, M. van den Heuvel, M. Kardolus, and P. Bauer, "A 10 kW Solar-Powered Bidirectional EV Charger Compatible With Chademo and COMBO," IEEE Transactions on Power Electronics, vol. 34, no. 2, pp. 1082–1098, Feb. 2019, doi: https://doi.org/10.1109/tpel.2018.2829211.

[25] M. O. Badawy et al., "Design and Implementation of a 75-kW Mobile Charging System for Electric Vehicles," IEEE Transactions on Industry Applications, vol. 52, no. 1, pp. 369–377, Jan. 2016, doi: https://doi.org/10.1109/tia.2015.2469775.

[26] U. B S, V. M. Khadkikar, H. Zeineldin, S. Singh, H. Otrok, and R. Mizouni, "Direct Electric Vehicle to Vehicle (V2V) Power Transfer Using On-board Drivetrain and Motor Windings,"

IEEE Transactions on Industrial Electronics, pp. 1–1, 2021, doi: https://doi.org/10.1109/tie.2021.3121707.
[27] G. Qiu and Vinod Khadkikar, "Electric Vehicle-to-Vehicle (V2V) Energy Transfer Using Motor Inverter and Winding," IEEE Transactions on Transportation Electrification, vol. 11, no. 5, pp. 11967–11976, Jun. 2025, doi: https://doi.org/10.1109/tte.2025.3584550.
[28] G. Qiu, V. Khadkikar, and B. Zahawi, "Capacitively Isolated Dual Active Bridge Converter for On-Board Charger Applications," IEEE Transactions on Industrial Electronics, vol. 72, no. 6, pp. 5833–5845, Jun. 2025, doi: https://doi.org/10.1109/tie.2024.3497328.
[29] S. Taghizadeh, M. J. Hossain, N. Poursafar, J. Lu, and G. Konstantinou, "A Multifunctional Single-Phase EV On-Board Charger With a New V2V Charging Assistance Capability," IEEE Access, vol. 8, pp. 116812–116823, 2020, doi: https://doi.org/10.1109/access.2020.3004931.
[30] A. Shafiqurrahman, B. S. Umesh, N. A. Sayari, and V. Khadkikar, "Electric Vehicle-to-Vehicle Energy Transfer Using On-Board Converters," IEEE Transactions on Transportation Electrification, vol. 9, no. 1, pp. 1263–1272, Mar. 2023, doi: https://doi.org/10.1109/TTE.2022.3172029.
[31] Y. Xu, M. Hu, C. Fu, K. Cao, Z. Su, and Z. Yang, "State of Charge Estimation for Lithium-Ion Batteries Based on Temperature-Dependent Second-Order RC Model," Electronics, vol. 8, no. 9, p. 1012, Sep. 2019, doi: https://doi.org/10.3390/electronics8091012.
[32] M.-K. Tran, A. DaCosta, A. Mevawalla, S. Panchal, and M. Fowler, "Comparative Study of Equivalent Circuit Models Performance in Four Common Lithium-Ion Batteries: LFP, NMC, LMO, NCA," Batteries, vol. 7, no. 3, p. 51, Jul. 2021, doi: https://doi.org/10.3390/batteries7030051.
[33] Mounika Reddimalla, Srinivasan Pradabane and K. Dahal, "Electric Vehicle to Vehicle (V2V) Power Transfer with On-Board Network and Capacitor-Link," 2024 Third International Conference on Power, Control and Computing Technologies (ICPC2T), Raipur, India, 2024, pp. 565-568, doi: 10.1109/ICPC2T60072.2024.10474760.

Mounika Reddimalla received the B.Tech. degree in Electrical and Electronics Engineering from SR Engineering College, India, in 2015, and the M.Tech. degree in Power Electronics and Drives from the National Institute of Technology, India, in 2020. She is currently pursuing the Ph.D. degree in Electrical Engineering at the National Institute of Technology, with a research focus on electric vehicle battery charging systems. Her research interests include electric vehicle battery charging systems, DC–DC converters, and model predictive control techniques.

Srinivasan Pradabane received the bachelor's degree in electrical and electronics engineering from Pondicherry University, Pondicherry, in 2005. He earned his master's degree in Power Electronics and Drives from Anna University, Chennai, in 2008 and his doctoral degree in Electrical Engineering in 2016 from the National Institute of Technology Warangal, India. He has been with the faculty of Electrical Engineering, National Institute of Technology Warangal, since 2012. Dr. Srinivasan Pradabane received the Erasmus-Mundus Post-Doctoral Research Fellowship and completed his PDF at the AVCN research center, University of the West of Scotland, UK, during 2017-2018. Later he received the European Union's transnational researcher fellowship award and visited the SINTEF energy research laboratory at NTNU, Trondheim, Norway. He published several articles in international journals and conferences. His research interests include DC drives, AC drives, electric propulsion technologies, integration of renewables, digital instrumentation & control, and driver circuit design.